Artery active mechanical response: High order finite element implementation and investigation

Zohar Yosibash * and Elad Priel [1]

Dept. of Mechanical Engrg., Ben-Gurion Univ. of the Negev, Beer-Sheva, 84105, Israel

Abstract

The active mechanical response of an artery wall resulting from the contraction of the smooth muscle cells (SMCs) is represented by a strain energy function (SEDF) that augments the passive SEDF recently reported in Yosibash Z. and Priel E., "p-FEMs for hyperelastic anisotropic nearly incompressible materials under finite deformations with applications to arteries simulation", *Int. Jour. Num. Meth. Eng.*, **88**:11521174, 2011. The passive-active hyperelastic, anisotropic, nearly-incompressible problem is solved using high-order finite element methods (p-FEMs). A new iterative algorithm, named "p-prediction", is introduced that accelerates considerably the Newton-Raphson algorithm when combined with p-FEMs. Verification of the numerical implementation is conducted by comparison to problems with analytic solutions and the advantages of p-FEMs are demonstrated by considering both degrees of freedom and CPU.

The passive and active material parameters are fitted to bi-axial inflation-extension tests conducted on rabbit carotid arteries reported in Wagner H.P. and Humphrey J.D., "Differential passive and active biaxial mechanical behavior of muscular and elastic arteries: Basilar versus common carotid", *Jour. Biomech. Eng.*, **133**, 2011. Article number: 051009. Our study demonstrates that the proposed SEDF is capable of describing the coupled passive-active response as observed in experiments. Artery-like structures are thereafter investigated and the effect of the activation level on the stress and deformation are reported. The active contribution reduces overall stress levels across the artery thickness and along the artery inner boundary.

Keywords: active response; p-FEM; artery; anisotropic Neo-Hooke material; hyperelasticity

* Corresponding author: zohary@bgu.ac.il

[1] Equal contribution

1 INTRODUCTION

Artery walls are anisotropic and nearly incompressible and consist of two main thin layers made of an elastin matrix embedded with stiff collagen fibers and smooth muscle cells (SMCs). In addition to the passive mechanical response due to the elastin and collagen fibers (well investigated in past studies), the SMCs contract in response to chemical stimulus thereby augment the passive response. Experiments show that the amount of tension generated by the SMCs is a function of the concentration of the chemical stimulus (does-tension relation) and the amount of stretch exerted on the muscle fiber (tension-stretch relation) [1].

Artery walls are considered as being hyperelastic, thus a strain energy density function (SEDF) is sought which determines the constitutive equation (stress-strain relationship). Numerous studies propose different SEDFs for the passive mechanical response [2,3,4]. Some are phenomenological based, so the SEDFs are formulated to result in a stress-strain response that mimics the experimentally observed response [2], or semi-structural [5,6] in which some terms in the SEDF are related to the tissue microstructure. A fully-structural model, in which each component of the artery wall is modeled, individually, best describes the overall passive response, see e.g. the recent work by Hollander et al. [6]. However, fully structural models are very difficult to formulate because they require knowledge of arterial microstructure which is in most cases unavailable. Therefore, semi-structural models are preferred, and herein we modify the semi-structural *incompressible* hyperelastic SEDF by Holzapfel et. al [5] for the passive part of the artery-wall response.

The active response and its numerical treatment were scarcely addressed in past publications comparing to publications on the passive response. One of the early works on the subject is by Rachev&Hayashi [7] in which the SMCs contribution was considered by an additional term to the Cauchy stress in the circumferential direction. The magnitude of the added stress depends on the chemical concentration and the circumferential stretch ratio. There, no clear relation was provided between the concentration of the stimulating chemical and the developed active stress. The study showed that incorporation of SMCs resulted in a reduction of the circumferential Cauchy stresses. The “added stress” proposed in [7] was utilized by Masson et al [8] to model the active response and to fit active material parameters from in-vivo monitoring of the time dependent pressure response of a human carotid artery, assuming as in [7], that the SMCs fibers were circumferentially oriented. A different functional representation for the added active stress was used by Wagner&Humphrey [9] for simulation of inflation-extension experiments on the basilar and common carotid arteries of New-Zealand white rabbits. The functional representation for tension-dose relation was more specific, enabling the modeling of partial SMCs contraction. An incompressible one-layer cylindrical tube-like artery undergoing pure radial deformation (enabling an analytical solution to be obtained) was considered.

Another method of introducing the SMCs effect in the constitutive model is through an "active-SEDF", see e.g., Zulliger et al. [10] and Murtada et al. [11]. The active-SEDF proposed in [10] does not incorporate the tension-dose relation and focuses on the passive, normal tone state (for which the pointwise activation level takes the form of Gaussian distribution function) and then on the maximum SMCs contraction. This results in a linear stress-strain relationship for maximal contracted SMCs thus it is only suited for the ascending part of the tension-stretch curve. The active-SEDF in [11] is based on a micro-mechanical approach so that the activation level is determined by a chemical kinetics model with an internal time-dependent variable, requiring the determination of many material properties. Schmitz and Bol [12] incorporated in the finite element (FE) framework an active-SEDF similar to the one in [11]. Uniaxial strip experiments on porcine medial strips reported by Herlihy&Murphy [13] under passive and active response were used to fit the active material parameters together with the collagen fiber dispersion reported by Dahl et al. [14] for the fit of the passive material parameters. Good agrement between the predicted and experimental results is reported, but the methods were not extended to artery-like structures and were restricted to strip specimens. It must also be noted that in [12] the implementation of the SEDF in the framework of FEs is not described and thus not verified.

In [15] the p-version of the FE method (p-FEM) was shown to perform very well for modeling the passive-response of artery-like structures and that slight compressibility which is mostly neglected in past studies was taken into consideration. Here we develop a new active-SEDF (aimed at augmenting the passive-SEDF in [15]) that is easily incorporated in the framework of p-FEMs. The use of p-FEMs based on the displacement formulation is motivated by the recent results [16,17,18,15] showing their advantages over conventional h-FEMs. p-FEMs were shown to be highly-efficiency for the analysis of isotropic hyperelastic materials and are locking-free for nearly incompressible Neo-Hook isotropic hyperelastic materials. These advantages in addition to the robustness of the p-FEM with respect to large aspect ratios and distortion of the elements, makes it especially attractive for modeling biological tissues as arteries. To the best of our knowledge this is the first study that uses p-FEMs to investigate the passive-active artery response. We present several "benchmark" problems used to verify our numerical implementation and demonstrate the superiority of p-FEMs over traditional h-FEMs in terms of degrees-of-freedom (DOFs) and CPU. A novel method, intrinsic to the hierarchic property of the p-shape functions, is exploited here to expedite the Newton-Rahpson algorithm and dramatically reduce computational time. Following the verification of our methods we use experimental inflation-extension observations reported by Wagner&Humphrey [9] to fit the material parameters for the passive and active SEDFs.

In section 2 the notations and the derivation of the active-SEDF are outlined and the ingredients required for implementation of the active model in the FE framework are explicitly presented. Three problems with analytic solution are utilized in sec-

tion 3 to verify our numerical implementation and to investigate the performance of the p- and h-FEMs. Fitting of passive and active model material parameters to experiments is outlined in section 4. There we also investigate the p-FEM performance for a more realistic bi-layer artery-like structure. In section 5 we emphasize the effect of the various active parameters on the artery wall. We summarize our work and draw several conclusions in section 6.

2 NOTATIONS AND IMPLEMENTATION OF AN ACTIVE-SEDF IN THE FRAMEWORK OF FEMs

The point of departure is a brief description of our notations for a fiber reinforced hyper-elastic material. The basic quantity is the deformation gradient $\boldsymbol{F} = \mathrm{Grad}\ \boldsymbol{x}(\boldsymbol{X}, t) = \partial x^k(X^1, X^2, X^3, t)/\partial X^K \boldsymbol{g}_i \otimes \boldsymbol{G}^K$, where $\boldsymbol{x}(\boldsymbol{X}, t)$ defines the placement of the point $\boldsymbol{X}$ at time t. X^K, $k = 1, 2, 3$, are the material (reference) coordinates, $\boldsymbol{g}_i$ are the tangent and $\boldsymbol{G}^K$ the gradient vectors in the current and the reference configuration. Customary, the displacement vector $\boldsymbol{U}(\boldsymbol{X}, t) \stackrel{\text{def}}{=} (U_X, U_Y, U_Z)^T$ is introduced, i.e. $\boldsymbol{x} = \boldsymbol{X} + \boldsymbol{U}(\boldsymbol{X}, t)$, and with this notation $\boldsymbol{F} = \boldsymbol{I} + \mathrm{Grad}\ \boldsymbol{U}(\boldsymbol{X}, t)$. We interchange X^1, X^2, X^3 with X, Y, Z when appropriate. A general strain-energy density function (SEDF) for an isotropic hyperelastic material with two families of fibers used to model the passive response is denoted by, $\psi_{passive}(\boldsymbol{C}, \hat{\boldsymbol{M}}_0, \hat{\boldsymbol{M}}_1) = \Psi_{passive}(\mathrm{I}_{\boldsymbol{C}}, \mathrm{II}_{\boldsymbol{C}}, \mathrm{III}_{\boldsymbol{C}}, \mathrm{IV}_{\boldsymbol{C}}, \mathrm{VI}_{\boldsymbol{C}})$, following Holzapfel et al. [5]. It depends on the invariants of the right Cauchy-Green tensor $\boldsymbol{C} = \boldsymbol{F}^T\boldsymbol{F} = (\boldsymbol{I} + \mathrm{Grad}\boldsymbol{U})^T\ (\boldsymbol{I} + \mathrm{Grad}\boldsymbol{U})$, and two unit direction vectors along collagen fiber directions $\hat{\boldsymbol{M}}_0$, and $\hat{\boldsymbol{M}}_1$. For example, using the Cartesian coordinate system in Figure 1, the fibers directions are $\hat{\boldsymbol{M}}_0 = (\sin\beta, -\cos\beta\frac{Y}{\sqrt{Y^2+Z^2}}, \cos\beta\frac{Z}{\sqrt{Y^2+Z^2}})^T$, $\hat{\boldsymbol{M}}_1 = (-\sin\beta, -\cos\beta\frac{Y}{\sqrt{Y^2+Z^2}}, \cos\beta\frac{Z}{\sqrt{Y^2+Z^2}})^T$. The invariants of the Cauchy-Green tensor are

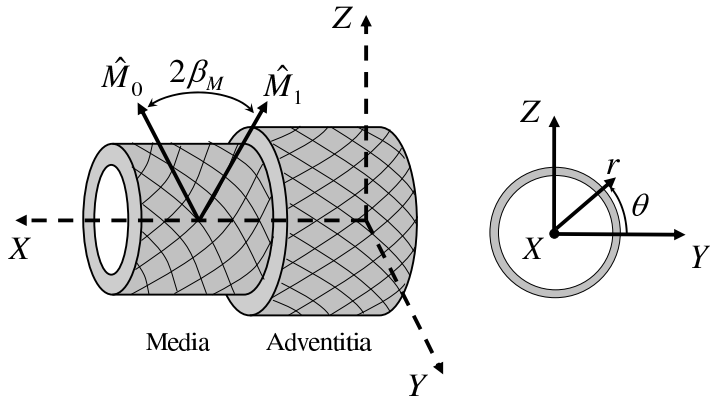

Fig. 1. Coordinate system in a typical artery.

$$\mathrm{I}_{\boldsymbol{C}} = tr\boldsymbol{C}, \qquad \mathrm{II}_{\boldsymbol{C}} = \frac{1}{2}((tr\boldsymbol{C})^2 - tr\boldsymbol{C}^2), \qquad \mathrm{III}_{\boldsymbol{C}} = \det \boldsymbol{C} = (\det \boldsymbol{F})^2 \stackrel{\text{def}}{=} J^2, \tag{1}$$

where $tr\boldsymbol{C}$ symbolizes the trace operator and the invariants that represent stretch in the fiber directions are

$$\mathrm{IV}_{\boldsymbol{C}} = \hat{\boldsymbol{M}}_0 \cdot \boldsymbol{C} \cdot \hat{\boldsymbol{M}}_0, \qquad \mathrm{VI}_{\boldsymbol{C}} = \hat{\boldsymbol{M}}_1 \cdot \boldsymbol{C} \cdot \hat{\boldsymbol{M}}_1, \tag{2}$$

Following [5] we consider a strain-energy density function composed of three parts for modeling the passive response, an isochoric isotropic and a volumetric isotropic Neo-Hook parts representing the elastic matrix, and a transversely isotropic part representing the collagen fibers in the artery wall

$$\Psi_{passive}(\mathrm{I}_{\boldsymbol{C}}, \mathrm{III}_{\boldsymbol{C}}, \mathrm{IV}_{\boldsymbol{C}}, \mathrm{VI}_{\boldsymbol{C}}) = [\Psi_{isoch}(\mathrm{I}_{\boldsymbol{C}}, \mathrm{III}_{\boldsymbol{C}}) + \Psi_{vol}(\mathrm{III}_{\boldsymbol{C}})] + \Psi_{fibers}(\mathrm{IV}_{\boldsymbol{C}}, \mathrm{VI}_{\boldsymbol{C}}), \tag{3}$$

The isochoric isotropic and volumetric isotropic parts are represented by a nearly incompressible Neo-Hookean SEDF:

$$\Psi_{isoch} = c_1(\mathrm{I}_{\boldsymbol{C}}\mathrm{III}_{\boldsymbol{C}}^{-1/3} - 3), \quad \Psi_{vol} = \frac{1}{D_1}(\mathrm{III}_{\boldsymbol{C}}^{1/2} - 1)^2 \tag{4}$$

c_1 and D_1 are constants related to the shear modulus μ and to the bulk modulus κ

$$c_1 = \frac{\mu}{2}, \qquad D_1 = \frac{2}{\kappa}. \tag{5}$$

The transversely isotropic part for modeling the collagen fiber contribution is [19]:

$$\begin{aligned} \Psi_{fibers} = & \frac{k_1}{2k_2}\left[\exp\left[k_2\left(\mathrm{IV}_{\boldsymbol{C}} - 1\right)^2\right] - 1\right] \\ & + \frac{k_1}{2k_2}\left[\exp\left[k_2\left(\mathrm{VI}_{\boldsymbol{C}} - 1\right)^2\right] - 1\right], \quad \mathrm{IV}_{\boldsymbol{C}}, \mathrm{VI}_{\boldsymbol{C}} \geq 1 \end{aligned} \tag{6}$$

Remark 1 *In some publications Ψ_{fibers} is expressed in terms of the invariants of the unimodular right Cauchy-Green tensor $\overline{\boldsymbol{C}} = (\det \boldsymbol{C})^{-1/3}\boldsymbol{C}$, i.e., $IV_{\overline{\boldsymbol{C}}} = IV_{\boldsymbol{C}}III_{\boldsymbol{C}}^{-1/3}$, $VI_{\overline{\boldsymbol{C}}} = VI_{\boldsymbol{C}}III_{\boldsymbol{C}}^{-1/3}$ (see [5]). This representation is inappropriate because no stresses are generated when an unimodular deformation is prescribed resulting in a homogeneous deformation that stretches the collagen fibers.*

For modeling the active response we construct a SEDF based on [7]. The first Piola-Kirchhoff stress component due to SMCs contraction was found to be proportional to the concentration of the vasoconstrictor $[A]$, as well as the stretch ratio in the SMCs-fibers direction $\hat{\boldsymbol{M}}_{MF}$, denoted by λ_f:

$$P_{ff}^{active} = S([A])f(\lambda_f) \tag{7}$$

where $S([A])$ is the tension-dose relationship and $f(\lambda_f)$ is the tension-stretch relation. The tension-dose relationship is usually available from ring-tests, as given for

example in [1], so that:

$$S([A]) = S_{max} \frac{[A]^m}{[A]^m + EC_{50}^m} \tag{8}$$

where m is the slope parameter, S_{max} the maximum value of contraction (saturation level) and EC_{50} is the concentration at which 50% of maximum generated tension is obtained. In Figure 2 a representative tension-dose relation is presented. It shows

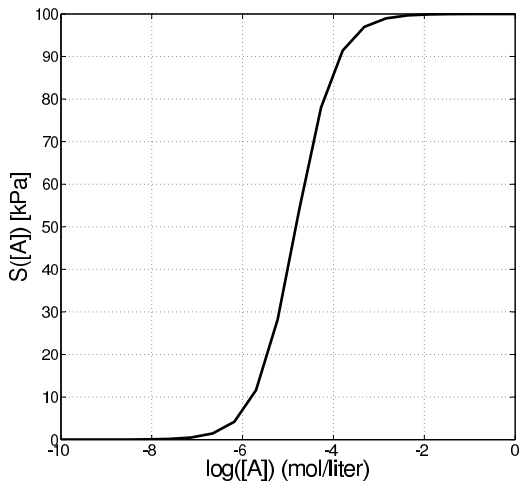

Fig. 2. Representative tension-dose relation using $EC_{50} = 0.000015\ [mol/liter]$, $m = 1$ taken from [1] and $S_{max} = 100\ kPa$ taken from [7].

that under a vasoconstrictor threshold concentration no induced active response is generated and on the other end the active response reaches a saturation level beyond a given vasoconstrictor concentration.

The tension-stretch relation is adopted from the work by Rachev&Hayashi [7], see e.g. Figure 11:

$$f(\lambda_f) = \begin{cases} \left[1 - \left(\frac{\lambda_m - \lambda_f}{\lambda_m - \lambda_0}\right)^2\right], & \lambda_1 > \lambda_f > \lambda_0 \\ 0, & Otherwise \end{cases} \tag{9}$$

with λ_m being the stretch at which maximum contraction is possible and λ_0 and $\lambda_1 = \lambda_0 + 2(\lambda_m - \lambda_0)$ being the minimum and maximum stretches at which contraction can be generated. This relationship is obtained from experiments at saturation levels so for λ_m:

$$P_{ff}^{active} = S_{max} \tag{10}$$

Inserting (8) and (9) in (7) one obtains:

$$P_{ff}^{active} = \begin{cases} S_{max} \frac{[A]^m}{[A]^m + EC_{50}^m} \left[1 - \left(\frac{\lambda_m - \lambda_f}{\lambda_m - \lambda_0}\right)^2\right], & \lambda_1 > \lambda_f > \lambda_0 \\ 0, & Otherwise \end{cases} \tag{11}$$

Remark 2 *The expression given in* (11) *results in different active stress values for the same chemical concentration provided that the SMCs are under different stretch ratios as demonstrated in experiments [13].*

Defining the direction of the SMCs after deformation as $\boldsymbol{m}_{MF}$, one can compute λ_f from the initial fiber direction and the right Cauchy-Green deformation tensor, see [20, (6.200)]:

$$\lambda_f^2 = (\boldsymbol{m}_{MF})^T \cdot (\boldsymbol{m}_{MF}) = (\boldsymbol{F}\hat{\boldsymbol{M}}_{MF})^T \cdot (\boldsymbol{F}\hat{\boldsymbol{M}}_{MF}) = \hat{\boldsymbol{M}}_{MF} \cdot (\boldsymbol{C}\hat{\boldsymbol{M}}_{MF}) = \mathrm{IV}_{\boldsymbol{C}}^{MF} \tag{12}$$

Assuming the existence of an active-SEDF Ψ_{active}, the first Piola-Kirchhoff stress in the SMC-fiber direction can be derived directly from the SEDF [20, (16.47)]:

$$P_{ff}^{active} = \frac{\partial \psi_{active}}{\partial \lambda_f} \tag{13}$$

Inserting (11) in (13) then integrating, on may obtain an expression for ψ_{active}:

$$\psi_{active}(\lambda_f, [A]) = \begin{cases} S_{max} \frac{[A]^m}{[A]^m + EC_{50}^m} \left[\frac{(\lambda_m - \lambda_f)^3}{3(\lambda_m - \lambda_0)^2} + \lambda_f \right], & \lambda_1 > \lambda_f > \lambda_0 \\ 0, & Otherwise \end{cases} \tag{14}$$

Substituting (12) in (14), a general form of the active-SEDF is obtained:

$$\Psi_{active}(\mathrm{IV}_{\boldsymbol{C}}^{MF}, [A]) = \begin{cases} S_{max} \frac{[A]^m}{[A]^m + EC_{50}^m} \left[\frac{(\lambda_m - \sqrt{\mathrm{IV}_{\boldsymbol{C}}^{MF}})^3}{3(\lambda_m - \lambda_0)^2} + \sqrt{\mathrm{IV}_{\boldsymbol{C}}^{MF}} \right], & \lambda_1^2 > \mathrm{IV}_{\boldsymbol{C}}^{MF} > \lambda_0^2 \\ 0, & Otherwise \end{cases} \tag{15}$$

The dependency of Ψ_{active} on $\mathrm{IV}_{\boldsymbol{C}}^{MF}$ assures that the active stress is in the SMCs direction only, with zero components perpendicular to it. In Appendix A we demonstrate that for the incompressible case $(J = 1)$ the SEDF (15) results in the Cauchy stress term for the active response given in [7], even if the deformation of the tissue is not in the SMC fiber direction.

The passive-active SEDF is the sum of the passive and active SEDFs:

$$\Psi_{tissue} = \Psi_{passive} + \Psi_{active} \tag{16}$$

For the purposes of implementation in a finite element code it is necessary to obtain expressions for the second- Piola- Kirchhoff stress $\boldsymbol{S}$ and the elasticity tensor $\mathbb{C} = \frac{\partial \boldsymbol{S}}{\partial \boldsymbol{C}}$. In [15] explicit expressions for $\boldsymbol{S}_{passive}$ and $\mathbb{C}_{passive}$ are provided. Using (15) one obtains explicit expressions for the active components required.

$$\boldsymbol{S}_{active} = S_{max} \frac{[A]^m}{[A]^m + EC_{50}^m} \left(\mathrm{IV}_{\boldsymbol{C}}^{MF}\right)^{-\frac{1}{2}} \left(1 - \left(\frac{\lambda_m - \sqrt{\mathrm{IV}_{\boldsymbol{C}}^{MF}}}{\lambda_m - \lambda_0}\right)^2\right) \left[\hat{\boldsymbol{M}}_{MF} \otimes \hat{\boldsymbol{M}}_{MF}\right] \tag{17}$$

$$\mathbb{C}_{active} = S_{max}\frac{[A]^m}{[A]^m + EC_{50}^m}\left[2\left(\mathrm{IV}_{\boldsymbol{C}}^{MF}\right)^{-1}\frac{(\lambda_m - \sqrt{\mathrm{IV}_{\boldsymbol{C}}^{MF}})}{(\lambda_m - \lambda_0)^2}\right. \tag{18}$$
$$\left. - \left(\mathrm{IV}_{\boldsymbol{C}}^{MF}\right)^{-\frac{3}{2}}\left(1 - \left(\frac{\lambda_m - \sqrt{\mathrm{IV}_{\boldsymbol{C}}^{MF}}}{\lambda_m - \lambda_0}\right)^2\right)\right]\left[\hat{\boldsymbol{M}}_{MF}\otimes\hat{\boldsymbol{M}}_{MF}\right]\left[\hat{\boldsymbol{M}}_{MF}\otimes\hat{\boldsymbol{M}}_{MF}\right]$$

The expressions for $\boldsymbol{S}_{active}$ and $\mathbb{C}_{active}$ are necessary for the "tangent stiffness matrix" and "out of balance" vector at each Newton-Raphson iteration used in the FE framework:

$$\boldsymbol{S} = \boldsymbol{S}_{passive} + \boldsymbol{S}_{active}, \quad \mathbb{C} = \mathbb{C}_{passive} + \mathbb{C}_{active} \tag{19}$$

3 VERIFICATION OF THE IMPLEMENTATION

To verify our numerical implementation for the SMCs contribution we consider three "benchmark" problems for which an analytical solution can be computed. The first two problems denoted as A and B represent homogenous stretch and shear respectively while problem C represents an inhomogeneous deformation. For all problems we assume a Neo-Hook matrix embedded with SMC fibers in a $2 \times 2 \times 2\ mm^3$ cube. For problems A and B the two families of collagen fibers are also incorporated in the SEDF and the domain is defined by $\{(X,Y,Z)|\ 0 < X < 2,\ 0 < Y < 2,\ 0 < Z < 2\}$. For problem C the domain is defined by $\{(X,Y,Z)|\ 0 < X < 2,\ 0 < Y < 2,\ 1 < Z < 3\}$. The orientations of the collagen fiber families are $\hat{\boldsymbol{M}}_0 = [\cos\beta, -\sin\beta\sin\phi, \sin\beta\cos\phi]$, $\hat{\boldsymbol{M}}_1 = [\cos\beta, \sin\beta\sin\phi, -\sin\beta\cos\phi]$ and the SMC fiber orientation is $\hat{\boldsymbol{M}}_{MF} = [0, \cos\beta_{MF}, \sin\beta_{MF}]$ (Figure 3). The material parameters used in (4), (6) and (15) for problems A and B are $c_1 = 0.027\ MPa,\ D_1 = 30\ MPa^{-1}, k_1 = 0.00064\ MPa, k_2 = 3.54\ MPa$ and $\lambda_m = 1.4, \lambda_0 = 0.65, S([A]) = 0.05\ MPa$. The constant value $S([A]) = 0.05\ MPa$ assigned is attributed to normal basal tone according to Rachev&Hayashi [7]. In Table 1 we summarize the boundary conditions and exact solutions for problems A-C. The matrix and fiber material parameters used above represent the human coronary artery [21]. The fourth and sixth invariants in Table 1 for problems A are $\mathrm{IV}_{\boldsymbol{C}} = \mathrm{VI}_{\boldsymbol{C}} = \cos\beta^2 + \sin^2\beta(\sin^2\phi + a^2\cos^2\phi)$ and for problem B are $\mathrm{IV}_{\boldsymbol{C}} = \mathrm{VI}_{\boldsymbol{C}} = \cos\beta^2 + \sin^2\beta(1 - \sin 2\phi\sin\theta)$. The fourth invariant of the SMC for problem A is $\mathrm{IV}_{\boldsymbol{C}}^{MF} = \cos^2\beta_{MF} + a^2\sin^2\beta_{MF}$ and for problem B $\mathrm{IV}_{\boldsymbol{C}}^{MF} = \sin\theta\sin 2\beta_{MF} + 1$. These invariants are to be substituted in the expressions given in Table 1.

For problem C we assumed the SMCs are aligned along the Z direction and did not consider the collagen fibers so as to be able to obtain an analytical solution. To ensure equilibrium one must also apply the following body force $f_Z = -\frac{4c_1}{18}Z^{\frac{4}{3}} - \frac{20c_1}{18}Z^{-\frac{7}{3}} - \frac{1}{D_1 Z} - S([A])\left(\frac{\lambda_m - \sqrt{Z}}{\lambda_m - \lambda_0}\right)Z^{-1}$ with the first part associated with the passive component and the second part associated with the active component (deriva-

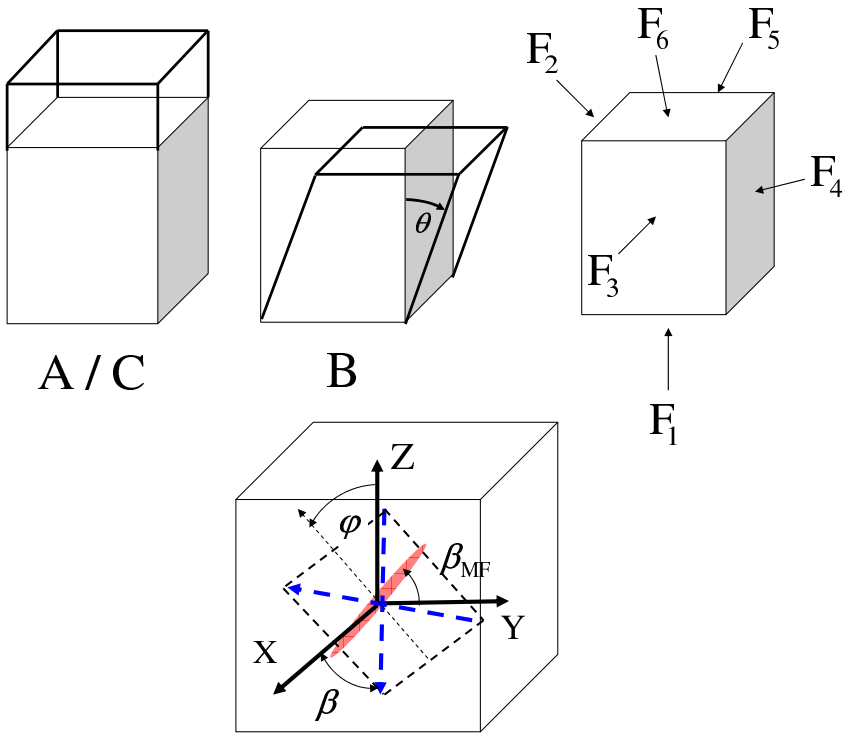

Fig. 3. Top Left and Middle: Domain and deformation for problems A/C, and B. Top Right: Face labeling used in Table 1. Bottom: Collagen and SMC fiber orientations.

tion of the body force are given in Appendix B). For problems A and B the analytic solution is obtained using one hexahedral element with $p = 1$ (due to the homogenous stress state higher p-levels are unnecessary). Several SMCs initial orientation angles were considered $\beta_{MF} = 0^0, 10^0, 30^0, 50^0, 70^0, 90^0$. Deformations of up to 100% were considered for problem A ($a = 2$) and shear angles of up to $\theta = 60^0$ for problem B. We used different combinations of β, β_{MF}, ϕ in our verification process. The exact solution was obtained in all cases using the p-FEM with ten load steps with an average of three equilibrium iterations for each load increment.

For problem C the deformation is inhomogeneous allowing to inspect the performance of p-FEMs compared to the conventional h-FEM for the coupled passive-active response. No commercial h-FEM code has the active model implemented thus we use our code for h-extensions also.

Remark 3 *Since we use our code for the h-extensions, in Appendix C we show that compared to the commercial finite element code Abaqus 6.8 E.F a maximum CPU factor of ≈ 2.5 between the run-times is obtained when a standard Neo-Hooke problem is considered.*

A p-extension on a uniform mesh with eight hexahedral elements is performed for the solution of problem C. At $p = 4$ already a relative error $||e(U)|| < 10^{-5}\%$ (see (20)) is obtained. For the h-extension the number of elements is increased, keeping fixed the polynomial degree over all elements with either $p = 1$ or $p = 2$. For the h-FEM ten equal load increments were used (the minimal number of load steps

required for convergence) and up to four equilibrium iterations were required for each load step.

For the p-FEM we use a novel iterative scheme denoted “p-prediction”. In this case for $p = 1$ the regular Newton-Raphson iterative algorithm is used. For a nearly-incompressible material, since the p-FEM encounters locking until $p = 4$, then the first p-FE solution starts at $p = 4$ by a regular Newton-Raphson algorithm. For $p \geq 2$ (and $p \geq 5$ for a nearly incompressible material), the converged solution at $p - 1$ is used as the ”initial guess” to the iterative algorithm, so that the entire load is not sub-divided in sub-loads. This results in a very fast convergence, usually with one load step. The “p-prediction” algorithm is shown in Figure 4.

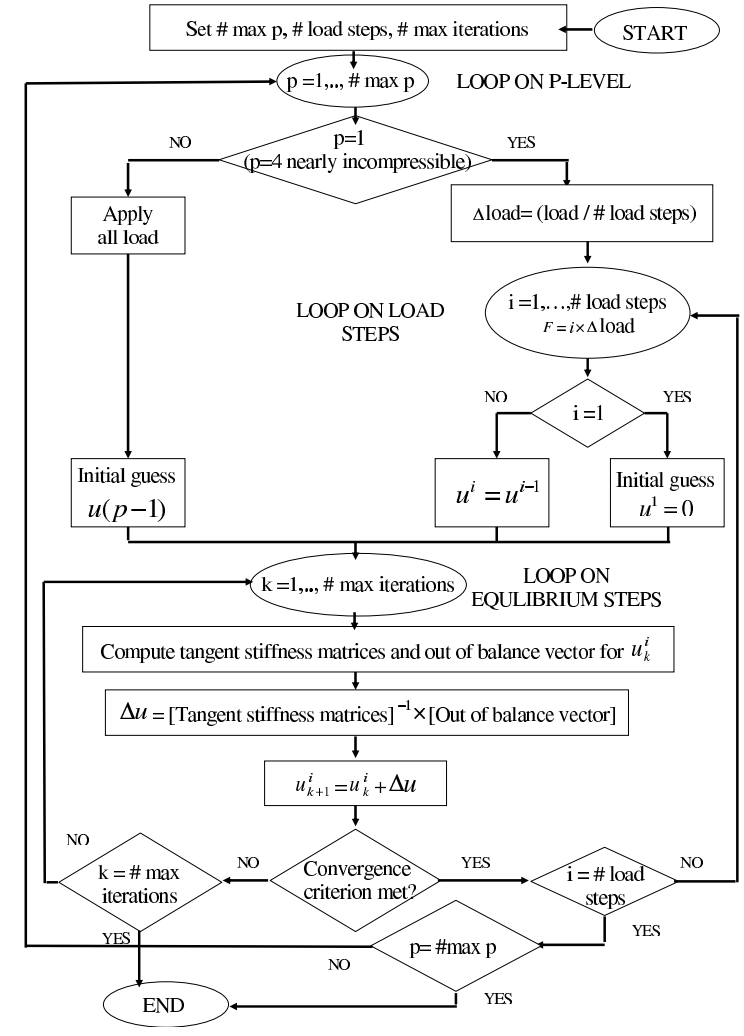

Fig. 4. The “p-prediction” algorithm.

To verify the numerical results we consider both global and pointwise values. The performance of p- and h-FEMs is demonstrated by inspecting the convergence of

the relative error in energy norm [22] .

$$||e(\mathcal{U})||(\%) = \sqrt{\frac{\int_\Omega \Psi(\boldsymbol{C}) d\Omega_{FE} - \int_\Omega \Psi(\boldsymbol{C}) d\Omega_{Exact}}{\int_\Omega \Psi(\boldsymbol{C}) d\Omega_{Exact}}} \times 100 \tag{20}$$

and pointwise by inspecting the convergence of U_z and σ_{zz}, σ_{xx} at points A and B (see Figure 5). In Figure 6 the convergence in the relative error in strain energy as

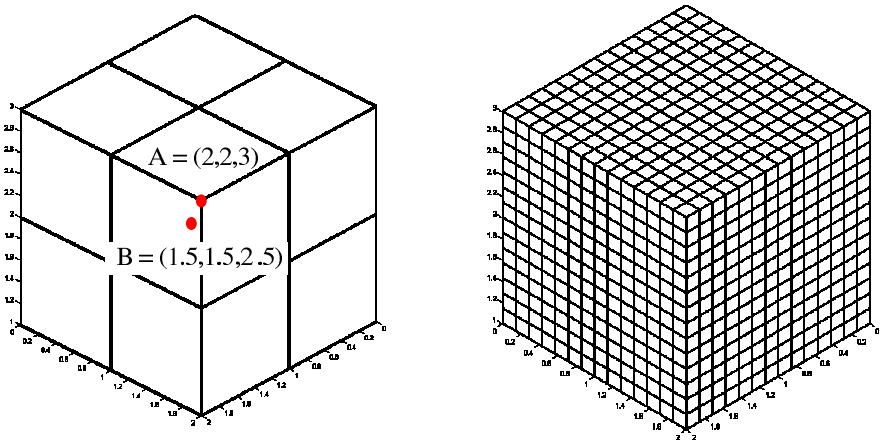

Fig. 5. Mesh used for problem C. Left: Uniform mesh for the p-FEM and points A and B. Right: Example of an uniform mesh for the h-FEM (2744 elements).

percentage, as a function of both DOFs and CPU is shown. The convergence of the relative error for the displacement and stresses at points A and B shown in Figure 5 is provided in Figures 7 to 9.

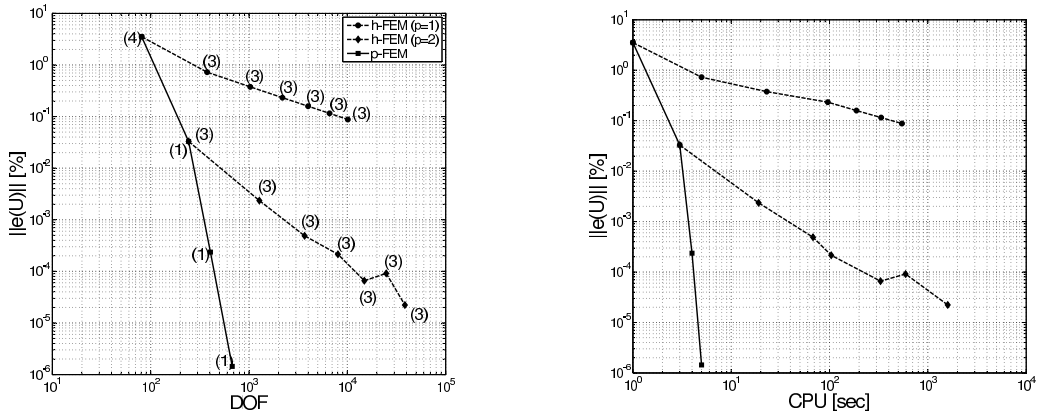

Fig. 6. Problem C: Convergence of the relative error in energy norm (the numbers in parentheses are number of load steps for convergence) for both p- and h-FEMs. Left: DOFs. Right: CPU.

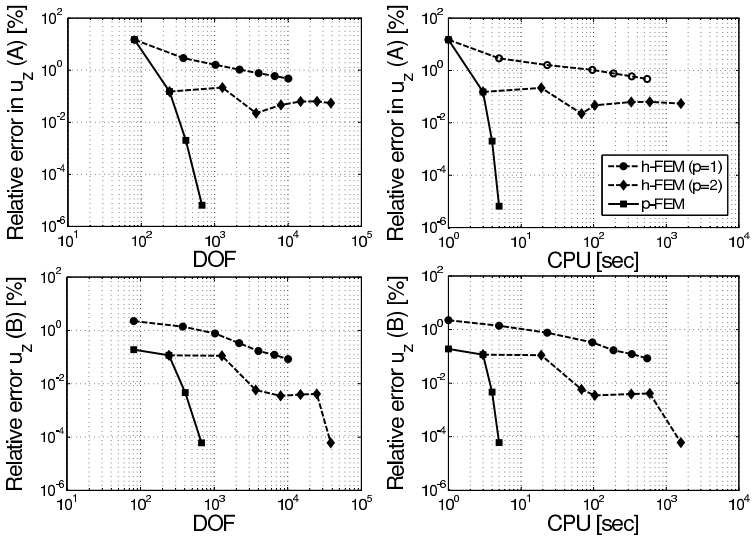

Fig. 7. Problem C: Convergence in U_Z for point A=(2,2,3) (top) and point B=(1.5,1.5,2.5)(bottom).

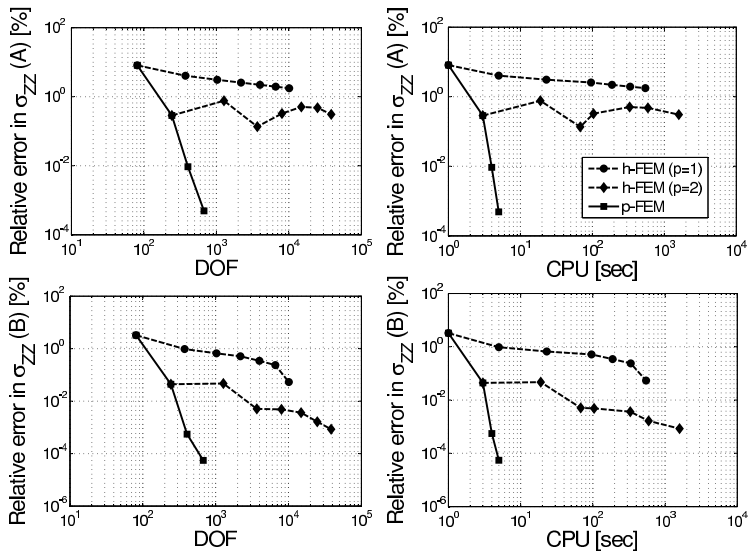

Fig. 8. Problem C: Convergence in σ_{zz} for point A=(2,2,3) (top) and point B=(1.5,1.5,2.5) (bottom).

As evident from Figures 6 to 9 the p-FEM is considerably more efficient for solving the passive-active mechanical response especially when computations of stress values are of interest.

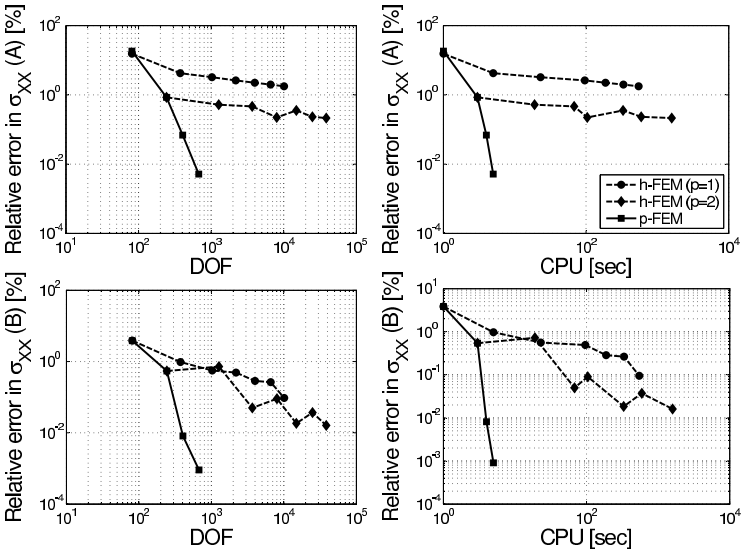

Fig. 9. Problem C: Convergence in σ_{xx} for point A=(2,2,3) (top) and point B=(1.5,1.5,2.5) (bottom).

Table 1. Tractions and exact solution for problem A.

Problem	Ω_0	Boundary conditions applied to faces F1-F6	Solution
A	$0 \leq X \leq 2$ $0 \leq Y \leq 2$ $0 \leq Z \leq 2$	$F1 : u_X = u_Y = u_Z = 0$ $F2 : t_Y = -\Big[\frac{2}{3}c_1\left(a^{-\frac{2}{3}} - a^{\frac{4}{3}}\right) + \frac{2}{D_1}\left(a^2 - a\right)$ $-4k_1\left[\mathrm{IV}_{\boldsymbol{C}} - 1\right] \times \left(\sin^2\beta\cos\phi\sin\phi\right)\exp^{k_2(\mathrm{IV}_{\boldsymbol{C}}-1)^2}$ $+S([A])\left(\mathrm{IV}_{\boldsymbol{C}}^{MF}\right)^{-\frac{1}{2}}\left(1 - \left(\frac{\lambda_m - \sqrt{\mathrm{IV}_{\boldsymbol{C}}^{MF}}}{\lambda_m - \lambda_0}\right)^2\right)\cos^2\beta_{MF}\Big]$ $t_Z = -\Big[4k_1\left[\mathrm{IV}_{\boldsymbol{C}} - 1\right] \times \left(\sin^2\beta\cos^2\phi\right)\exp^{k_2(\mathrm{IV}_{\boldsymbol{C}}-1)^2}$ $+S([A]) \cdot a\left(\mathrm{IV}_{\boldsymbol{C}}^{MF}\right)^{-\frac{1}{2}}\left(1 - \left(\frac{\lambda_m - \sqrt{\mathrm{IV}_{\boldsymbol{C}}^{MF}}}{\lambda_m - \lambda_0}\right)^2\right)\cos\beta_{MF}\sin\beta_{MF}\Big]$ $F3 : t_X = \frac{2}{3}c_1\left(a^{-\frac{2}{3}} - a^{\frac{4}{3}}\right) + \frac{2}{D_1}\left(a^2 - a\right)$ $+4k_1\left[\mathrm{IV}_{\boldsymbol{C}} - 1\right] \times \left(\cos^2\beta\right)\exp^{k_2(\mathrm{IV}_{\boldsymbol{C}}-1)^2}$ $F4 : t_Y = \frac{2}{3}c_1\left(a^{-\frac{2}{3}} - a^{\frac{4}{3}}\right) + \frac{2}{D_1}\left(a^2 - a\right)$ $+4k_1\left[\mathrm{IV}_{\boldsymbol{C}} - 1\right] \times \left(\sin^2\beta\cos\phi\sin\phi\right)\exp^{k_2(\mathrm{IV}_{\boldsymbol{C}}-1)^2}$ $+S([A])\left(\mathrm{IV}_{\boldsymbol{C}}^{MF}\right)^{-\frac{1}{2}}\left(1 - \left(\frac{\lambda_m - \sqrt{\mathrm{IV}_{\boldsymbol{C}}^{MF}}}{\lambda_m - \lambda_0}\right)^2\right)\cos^2\beta_{MF}\Big)$ $t_Z = \Big[4k_1\left[\mathrm{IV}_{\boldsymbol{C}} - 1\right] \times \left(\sin^2\beta\cos^2\phi\right)\exp^{k_2(\mathrm{IV}_{\boldsymbol{C}}-1)^2}$ $+S([A]) \cdot a\left(\mathrm{IV}_{\boldsymbol{C}}^{MF}\right)^{-\frac{1}{2}}\left(1 - \left(\frac{\lambda_m - \sqrt{\mathrm{IV}_{\boldsymbol{C}}^{MF}}}{\lambda_m - \lambda_0}\right)^2\right)\cos\beta_{MF}\sin\beta_{MF}$ $F5 : t_X = -\left(\frac{2}{3}c_1\left(a^{-\frac{2}{3}} - a^{\frac{4}{3}}\right) + \frac{2}{D_1}\left(a^2 - a\right)\right)$ $-4k_1\left[\mathrm{IV}_{\boldsymbol{C}} - 1\right] \times \left(\cos^2\beta\right)\exp^{k_2(\mathrm{IV}_{\boldsymbol{C}}-1)^2}$ $F6 : t_Z = \frac{4}{3}c_1\left(a^{\frac{1}{3}} - a^{\frac{5}{3}}\right) + \frac{2}{D_1}\left(a - 1\right)$ $+4k_1\left[\mathrm{IV}_{\boldsymbol{C}} - 1\right] \times \left(\sin^2\beta\cos^2\phi\right)\exp^{k_2(\mathrm{IV}_{\boldsymbol{C}}-1)^2}$ $+S([A])a\left(\mathrm{IV}_{\boldsymbol{C}}^{MF}\right)^{-\frac{1}{2}}\left(1 - \left(\frac{\lambda_m - \sqrt{\mathrm{IV}_{\boldsymbol{C}}^{MF}}}{\lambda_m - \lambda_0}\right)^2\right)\sin^2\beta_{MF}\Big)$ $t_Y = -4k_1 a\left[\mathrm{IV}_{\boldsymbol{C}} - 1\right] \times \left(\sin^2\beta\cos\phi\sin\phi\right)\exp^{k_2(\mathrm{IV}_{\boldsymbol{C}}-1)^2}$ $-S([A])\left(\mathrm{IV}_{\boldsymbol{C}}^{MF}\right)^{-\frac{1}{2}}\left(1 - \left(\frac{\lambda_m - \sqrt{\mathrm{IV}_{\boldsymbol{C}}^{MF}}}{\lambda_m - \lambda_0}\right)^2\right)\cos\beta_{MF}\sin\beta_{MF}$	$x = X, y = Y, z = aZ$ $u_X = 0$ $u_Y = 0$ $u_Z = Z(a-1)$

Continuation of Table 1: Tractions and exact solution for problem B.

Problem	Ω_0	Boundary conditions applied to faces F1-F6	Solution
B	$0 \leq X \leq 2$ $0 \leq Y \leq 2$ $0 \leq Z \leq 2$	$F1 : u_X = u_Y = u_Z = 0$ $F2 : t_Y = -\left(2c_1\left(cos^{-\frac{2}{3}}(\theta) - cos^{-\frac{8}{3}}(\theta)(1+sin^2(\theta))\right) + \frac{2}{D_1}\left(\frac{sin(\theta)}{cos(\theta)} - sin(\theta) + cos(\theta) - 1\right)\right)$ $+4k_1\left[\mathrm{IV}_{\boldsymbol{C}} - 1\right] \times e^{k_2(\mathrm{IV}_{\boldsymbol{C}}-1)^2} \sin^2\beta\left[\sin^2\phi - \sin\theta\sin\phi\cos\phi\right]$ $+S([A])\left(\mathrm{IV}_{\boldsymbol{C}}^{MF}\right)^{-\frac{1}{2}}\left(1 + \left(\frac{\lambda_m - \sqrt{\mathrm{IV}_{\boldsymbol{C}}^{MF}}}{\lambda_m - \lambda_0}\right)^2\right)\left[\cos^2\beta_{MF} + \sin\theta\sin\beta_{MF}\cos\beta_{MF}\right]\Bigg)$ $t_Z = -2c_1\left(cos^{-\frac{8}{3}}(\theta)sin(\theta) + cos^{\frac{1}{3}}(\theta) - cos^{-\frac{5}{3}}(\theta)\right) + \frac{2}{D_1}\left(\frac{sin(\theta)}{cos(\theta)} - sin(\theta) + cos(\theta) - 1\right)$ $-4k_1\left[\mathrm{IV}_{\boldsymbol{C}} - 1\right]\sin^2\beta\sin\phi\cos\phi\cos\theta \times \exp^{k_2(\mathrm{IV}_{\boldsymbol{C}}-1)^2}$ $+S([A])\left(\mathrm{IV}_{\boldsymbol{C}}^{MF}\right)^{-\frac{1}{2}}\left(1 + \left(\frac{\lambda_m - \sqrt{\mathrm{IV}_{\boldsymbol{C}}^{MF}}}{\lambda_m - \lambda_0}\right)^2\right)\cos\theta\cos\beta_{MF}\sin\beta_{MF}\Bigg)$ $F3 : t_X = \frac{2}{D_1}\left(cos^2(\theta) - cos(\theta)\right) + 4k_1\left[\mathrm{IV}_{\boldsymbol{C}} - 1\right]\cos^2\beta \times \exp^{k_2(\mathrm{IV}_{\boldsymbol{C}}-1)^2}$ $F4 : t_Y = 2c_1\left(cos^{-\frac{2}{3}}(\theta) - cos^{-\frac{8}{3}}(\theta)(1+sin^2(\theta))\right) + \frac{2}{D_1}\left(1 - cos^{-1}(\theta) + sin^2(\theta)(cos^{-1}(\theta) - 1)\right)$ $+4k_1\left[\mathrm{IV}_{\boldsymbol{C}} - 1\right] \times e^{k_2(\mathrm{IV}_{\boldsymbol{C}}-1)^2} \sin^2\beta\left[\sin^2\phi - \sin\theta\sin\phi\cos\phi\right]$ $+S([A])\left(\mathrm{IV}_{\boldsymbol{C}}^{MF}\right)^{-\frac{1}{2}}\left(1 + \left(\frac{\lambda_m - \sqrt{\mathrm{IV}_{\boldsymbol{C}}^{MF}}}{\lambda_m - \lambda_0}\right)^2\right)\left[\cos^2\beta_{MF} + \sin\theta\sin\beta_{MF}\cos\beta_{MF}\right]\Bigg)$ $t_Z = 2c_1\left(cos^{-\frac{8}{3}}(\theta)sin(\theta) + cos^{\frac{1}{3}}(\theta) - cos^{-\frac{5}{3}}(\theta)\right)\Big) + \frac{2}{D_1}\left(\frac{sin(\theta)}{cos(\theta)} - sin(\theta) + cos(\theta) - 1\right)\Big)$ $-4k_1\left[\mathrm{IV}_{\boldsymbol{C}} - 1\right]\sin^2\beta\sin\phi\cos\phi\cos\theta \times \exp^{k_2(\mathrm{IV}_{\boldsymbol{C}}-1)^2}$ $+S([A])\left(\mathrm{IV}_{\boldsymbol{C}}^{MF}\right)^{-\frac{1}{2}}\left(1 + \left(\frac{\lambda_m - \sqrt{\mathrm{IV}_{\boldsymbol{C}}^{MF}}}{\lambda_m - \lambda_0}\right)^2\right)\cos\theta\cos\beta_{MF}\sin\beta_{MF}\Bigg)$ $F5 : t_X = -\left(\frac{2}{D_1}\left(cos^2(\theta) - cos(\theta)\right)\right) - 4k_1\left[\mathrm{IV}_{\boldsymbol{C}} - 1\right]\cos^2\beta \times \exp^{k_2(\mathrm{IV}_{\boldsymbol{C}}-1)^2}$ $F6 : t_Z = 2c_1\left(cos^{\frac{1}{3}}(\theta) - cos^{-\frac{5}{3}}(\theta)\right) + \frac{2}{D_1}\left(cos(\theta) - 1\right)$ $4k_1\left[\mathrm{IV}_{\boldsymbol{C}} - 1\right]\sin^2\beta\sin^2\phi\cos\theta \times \exp^{k_2(\mathrm{IV}_{\boldsymbol{C}}-1)^2}$ $+S([A])\left(\mathrm{IV}_{\boldsymbol{C}}^{MF}\right)^{-\frac{1}{2}}\left(1 + \left(\frac{\lambda_m - \sqrt{\mathrm{IV}_{\boldsymbol{C}}^{MF}}}{\lambda_m - \lambda_0}\right)^2\right)\cos\theta\sin^2\beta_{MF}\Bigg)$ $t_Y = 2c_1 cos^{-\frac{5}{3}}(\theta)sin(\theta) + \frac{2}{D_1}\left(sin(\theta) - cos(\theta)sin(\theta)\right)$ $-4k_1\left[\mathrm{IV}_{\boldsymbol{C}} - 1\right]\sin^2\beta\sin\phi\cos\phi\cos\theta \times \exp^{k_2(\mathrm{IV}_{\boldsymbol{C}}-1)^2}$ $+S([A])\left(\mathrm{IV}_{\boldsymbol{C}}^{MF}\right)^{-\frac{1}{2}}\left(1 + \left(\frac{\lambda_m - \sqrt{\mathrm{IV}_{\boldsymbol{C}}^{MF}}}{\lambda_m - \lambda_0}\right)^2\right)\left[\sin\theta\sin^2\beta_{MF} + \sin\beta_{MF}\cos\beta_{MF}\right]\Bigg)$	$x = X, y = Y + Zsin(\theta)$ $z = Zcos(\theta)$ $u_X = 0$ $u_Y = Zsin(\theta)$ $u_Z = Z(cos(\theta) - 1)$

Continuation of Table 1: Tractions and exact solution for problem C.

Problem	Ω_0	Boundary conditions applied to faces F1-F6	Solution
C	$0 \leq X \leq 2$ $0 \leq Y \leq 2$ $1 \leq Z \leq 3$	$F1 : u_X = u_Y = u_Z = 0$ $F2 : t_Y = -\left(\frac{2}{3}c_1\left(Z^{-\frac{2}{6}} - Z^{\frac{4}{6}}\right) + \frac{2}{D_1}\left(Z - \sqrt{Z}\right)\right)$ $F3 : t_X = \frac{2}{3}c_1\left(Z^{-\frac{2}{6}} - Z^{\frac{4}{6}}\right) + \frac{2}{D_1}\left(Z - \sqrt{Z}\right)$ $F4 : t_Y = \frac{2}{3}c_1\left(Z^{-\frac{2}{6}} - Z^{\frac{4}{6}}\right) + \frac{2}{D_1}\left(Z - \sqrt{Z}\right)$ $F5 : t_X = -\left(\frac{2}{3}c_1\left(Z^{-\frac{2}{6}} - Z^{\frac{4}{6}}\right) + \frac{2}{D_1}\left(Z - \sqrt{Z}\right)\right)$ $F6 : t_Z = \frac{4}{3}c_1\left(Z^{\frac{1}{6}} - Z^{\frac{5}{6}}\right) + \frac{2}{D_1}\left(\sqrt{Z} - 1\right) + S([A])\left(1 + \left(\frac{\lambda_m - \sqrt{Z}}{\lambda_m - \lambda_0}\right)^2\right)$	$x = X, y = Y, z = \frac{2}{3}Z^{\frac{3}{2}} + \frac{1}{3}$ $u_X = 0$ $u_Y = 0$ $u_Z = \frac{2}{3}Z^{\frac{3}{2}} - Z + \frac{1}{3}$

4 FITTING MATERIAL PARAMETERS TO INFLATION-EXTENSION EXPERIMENTS

After verifying the FE implementation on simple problems for which an analytical solution may be derived, we investigate how well one may predict the passive-active response (using p-FEMs with the suggested SEDF), when compared to experimental observations. For this purpose, one needs to estimate the material properties using experiments in which multi-axial loadings (tension, extension, torsion) are applied on the distinct layers of the arteries in a passive state, and thereafter when the smooth muscle cells are activated. Publications detailing such experiments on arteries including geometrical data, precise loading conditions and detailed measured observations, are very rare, and usually only partial information is available. Here we use the recent publication by Wagner and Humphrey [9] in which inflation-extension experiments of carotid artery specimens harvested from the New Zealand rabbit are reported. The numerical performance of the p-FEM implementation on a more realistic artery is demonstrated after fitting the material parameters to the experiments in [9]. There, artery specimens were stretched to their observed in-vivo axial stretch $\lambda_x = 1.68$ and then an internal pressure was applied ($P = 7mmHg$ to $P = 120mmHg$) while measuring the outer diameter and axial force required to maintain the axial-stretch constant. These experiments were conducted for a pure passive state and thereafter when exposing the artery to increasing concentrations of the vasoconstrictor Endothelin-1 ($[A] = 10^{-10} - 10^{-7}[mol/liter]$).

We mimic the experiments by constructing a bi-layered cylindrical tube with a mesh and boundary condition shown in Figure 10. The inner and outer radial displacements, circumferential stress and energy norm were computed for p-levels $p = 1-8$ to ensure that the results are free of numerical errors. Since for all parameters examined, the values obtained at $p = 4$ are within less than 0.1% error compared to $p = 8$ results, we used in the subsequent computations a p-level of 4.

No data is provided in [9] on the ratio between the media thickness to the total wall thickness, thus we assume it to be $2/3$ as common in a muscular artery [21].

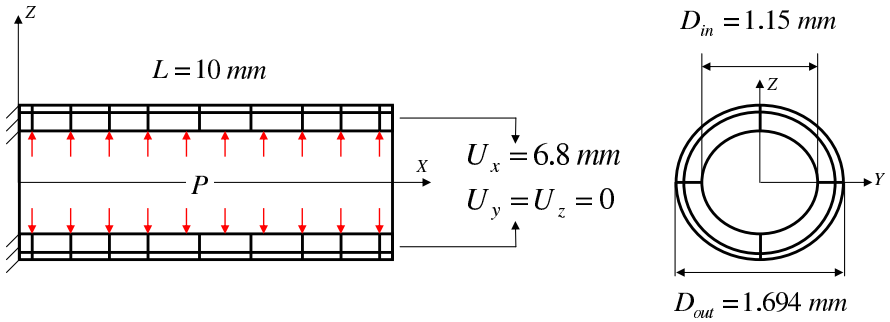

Fig. 10. Mesh and boundary conditions that mimic a bi-layered artery described in [9].

The material parameters for the passive response are first determined so that the

outer diameter and axial force measured correspond to the ones computed when the pre-stretch is applied and internal pressure is increased. The compressibility parameter D_1 is determined by assuming that under physiological pressure, the relative change of volume is $\approx 1\%$ as reported in [23] for the rabbit aorta. The fitted material properties for the passive response are provided in Table 2 and the comparison between the predicted response and the experimental observations is depicted in Figure 12 by the solid line.

Table 2
Material parameters fitted to a slightly compressible passive SEDF.

Layer	c_1 $[MPa]$	D_1 $[MPa^{-1}]$	k_1 $[MPa]$	k_2	β_M $[^0]$
Media	0.01	3	0.0006	1.2	± 20
Adventitia	0.005	3	0.0004	1.2	± 64

To determine the active material parameters we fitted the data for the tension-stretch and tension-dose relationship reported in [9] as presented in Figure 11. These parameters are summarized in Table 3.

Table 3
Material parameters fitted to the coupled passive-active SEDF.

λ_m	λ_0	S_{max} $[MPa]$	m	EC_{50} $[mol/liter]$
1.49	0.85	0.045	5.9	10^{-10}

Neither the density nor the orientation of SMCs is available, thus we assumed that these are uniformly distributed so a similar active response is obtained in the entire artery and that SMC are oriented circumferentially, i.e. $\beta_{MF} = 0$. With these assumptions, and using the already determined passive and active material properties, we predict the pressure-diameter and pressure-axial force response when the artery is activated by a vasoconstrictor. In Figure 12 we present the predicted response as compared to the experimental observations extracted from [9] for different internal pressures and a given axial stretch of $\lambda_x = 1.68$. The axial force is computed by the integral of the Cauchy stress over the deformed cross section area of the artery. One may observe that the passive-active predicted response is close to the experimental observations. However, below a pressure of about 40 mmHg in the passive state, and 70 mmHg in the active state, an unclear phenomenon in the experimental observations is visible, namely, the axial force increases as the pressure decreases. This phenomenon in the experimental observations in [9] is unclear to us and cannot be explained by the proposed SEDF.

An important experimental observation associated with the active response of the SMCs is the phenomenon of reduced contraction (at a fixed concentration of the

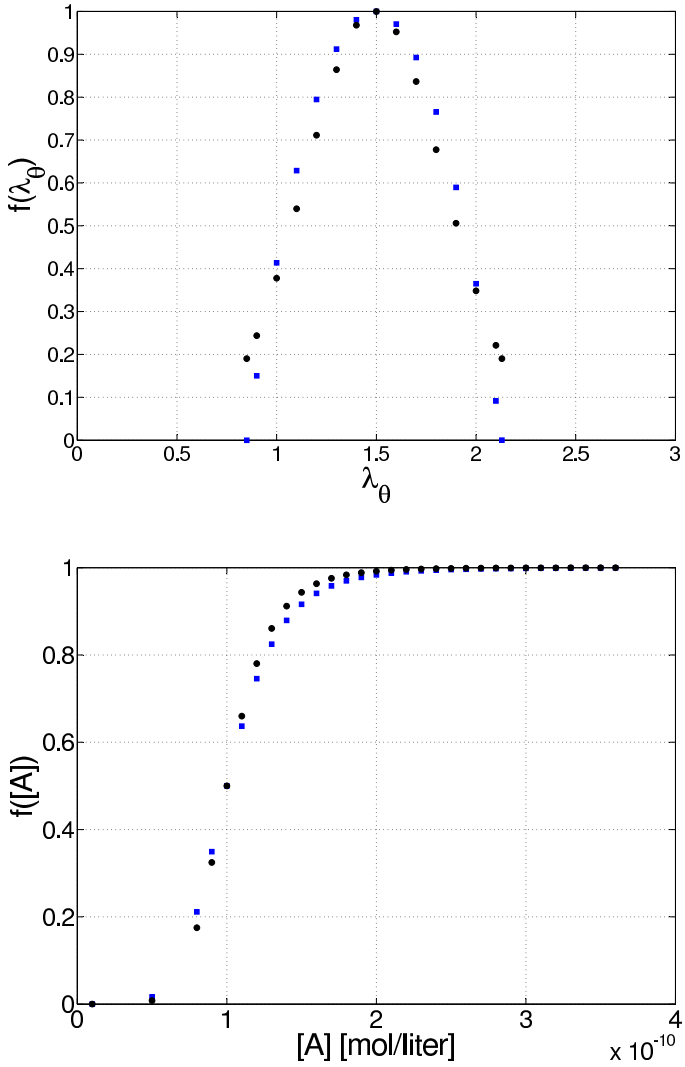

Fig. 11. Fitting of tension-stretch and tension-dose relationships: Circles - experimental results extracted from [9], Squares - fitted data using (9) and (8).

vasoconstrictor) beyond a given stretch ratio (λ_m). This observation is clearly shown by Herlihy&Murphy [13]. There uniaxial tension experiments of stimulated strips harvested from the media layer of the swine carotid artery are reported. In Appendix D we demonstrate that our analyses simulate well this phenomena.

4.1 Verification of the $p - FE$ implementation on a representative bi-layered artery

Using the fitted material parameters given in Tables 2 and 3 we consider the bi-layered artery having the dimensions and boundary conditions as in Figure 10. Since we only consider $\beta_{MF} = 0$, a circumferential segment can be used, and we

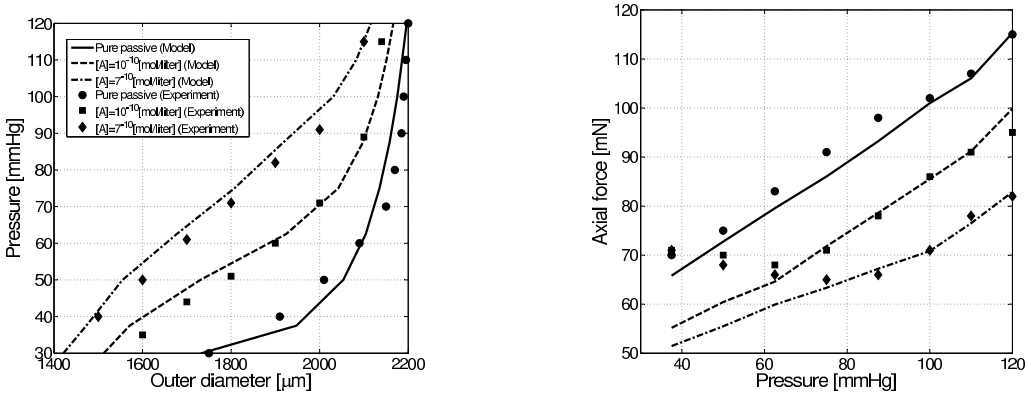

Fig. 12. Comparison of the predicted and experimental observed response of a New Zealand rabbit carotid artery in passive and passive-active states reported in [9]. Left: Diameter–pressure response at $X = 5\ mm$ for a constant $\lambda_x = 1.68$. Right: Pressure-axial force response.

chose one fourth with appropriate symmetry boundary conditions. A physiological pressure of $P = 100mmHg$ is applied on the internal surface and a SMC activation caused by a vasoconstrictor concentration $[A] = 10 \cdot 10^{-11}$. A "benchmark" solution is obtained by solving the problem using 240 hexahedral elements ($4 \times 6 \times 10$ in θ, R, X directions) and $p = 8$. The convergence in energy norm for the "benchmark" solution is given in Figure 13. The problem is solved also

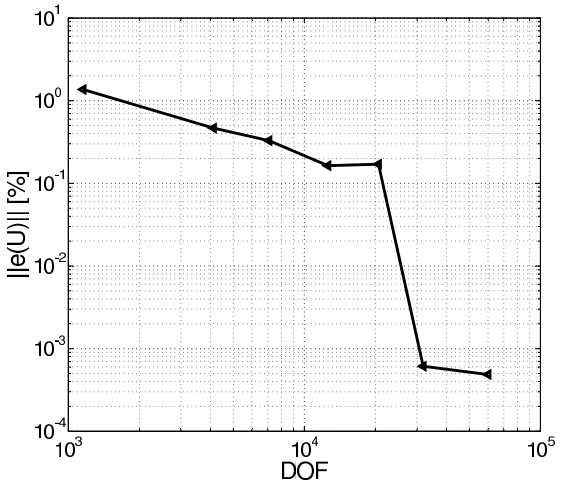

Fig. 13. Convergence in energy norm for $p = 1$ to 7 in comparison to the benchmark solution at $p = 8$.

by h-extension and p-extension with and without the p-prediction algorithm. In case of h-extension meshes with $12, 150, 300, 480, 1200, 4800$ elements were used, whereas for p-extensions we use a coarse mesh, see Figure 14. For both the h-FEM and p-FEM without p-prediction, the load was applied in thirty equal load steps. In Figures 1516 and 17 the convergence in energy norm, radial displacement and

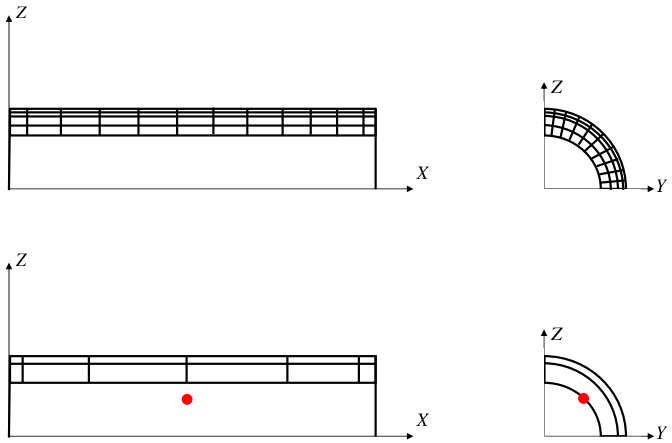

Fig. 14. Top: Representative h-FE mesh consisting of 480 elements. Bottom: Constant p-FE mesh consisting of 12 elements and the point of data extraction.

circumferential stress are presented. One may observe that the p-prediction algo-

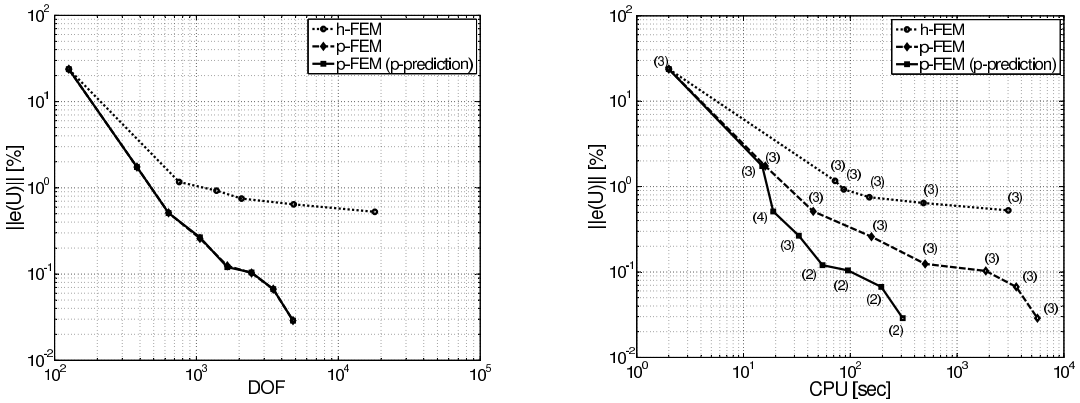

Fig. 15. Convergence in energy norm for the artery problem with the number of average equilibrium iterations in parenthesis.

rithm significantly reduces the computation time and that p-FEMs are by far more efficient than h-FEM, both in DOFs and CPU.

5 THE EFFECT OF SMCs ON THE MECHANICAL RESPONSE OF AN ARTERY

The bi-layered artery with boundary conditions and mesh similar to these presented in Figure 10 is used as the basis for the investigation of the SMCs-effects on the

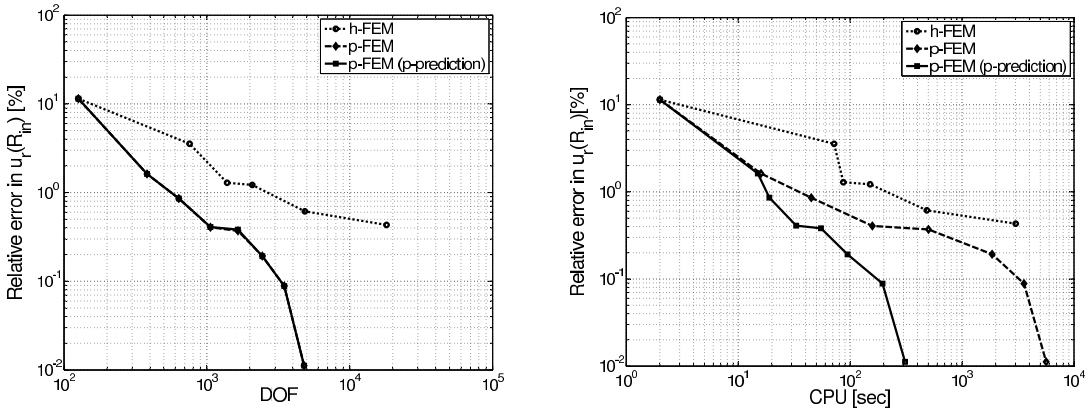

Fig. 16. Convergence in radial displacement at the point of interest for the artery problem.

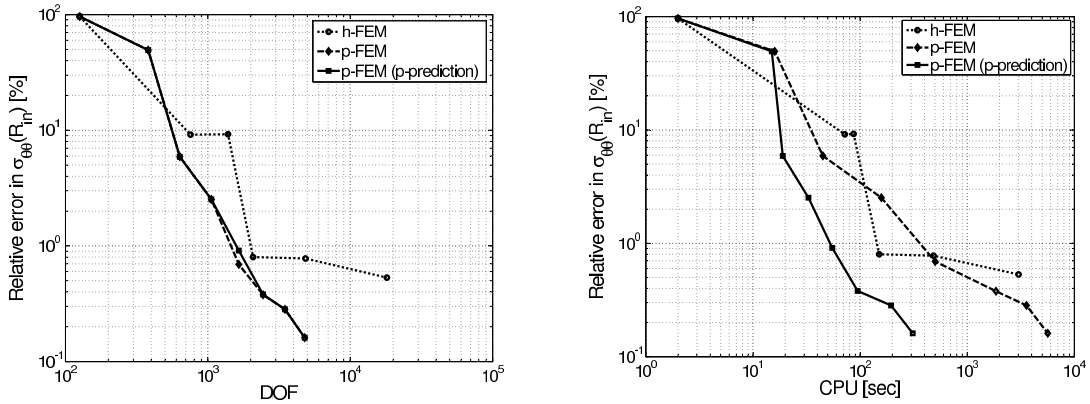

Fig. 17. Convergence in circumferential Cauchy stress at the point of interest for the artery problem.

mechanical response. The material parameters are those in Tables 2 and 3 and the SMCs are assumed to be oriented in the circumferential direction $\beta_{MF} = 0$. To investigate the effect of the vasoconstrictor concentration levels we increase $[A]$ from a pure passive state until saturation level $[A] = 10 \cdot 10^{-12},\ [A] = 8.3 \times 10^{-11},\ 10 \times 10^{-11},\ 12 \times 10^{-11},\ 10 \times 10^{-8} [mol/liter]$. The activation levels chosen represent values of $0, 25, 50, 75, 100\%$ on the tension-dose curve (Figure 11). To investigate the effect of the tension-stretch relation we fix the vasoconstrictor concentration at $[A] = 10 \cdot 10^{-11}$ and investigate different pressure values in the physiological range $P = 80, 100, 120\ mmHg$. In all cases the radial displacement and circumferential Cauchy stress across the artery wall thickness (at $X = 5$ mm) are computed. In Figure 18 the effect of increased activation level on the circumferential stress and stretch ratio is shown. The dashed vertical line in Figure 18-Top represents the media-adventitia-interface, whereas the horizontal dashed line in 18-Bottom represents the value of $\lambda_m = 1.49$. Figure 18 demonstrates that an increase in the concentration of the vasoconstrictor results in the "flattening" of the stress distribution across the artery wall. One may observe a decrease in the circumferential stress at the inner boundary of the media and an increase at the outer boundary of the me-

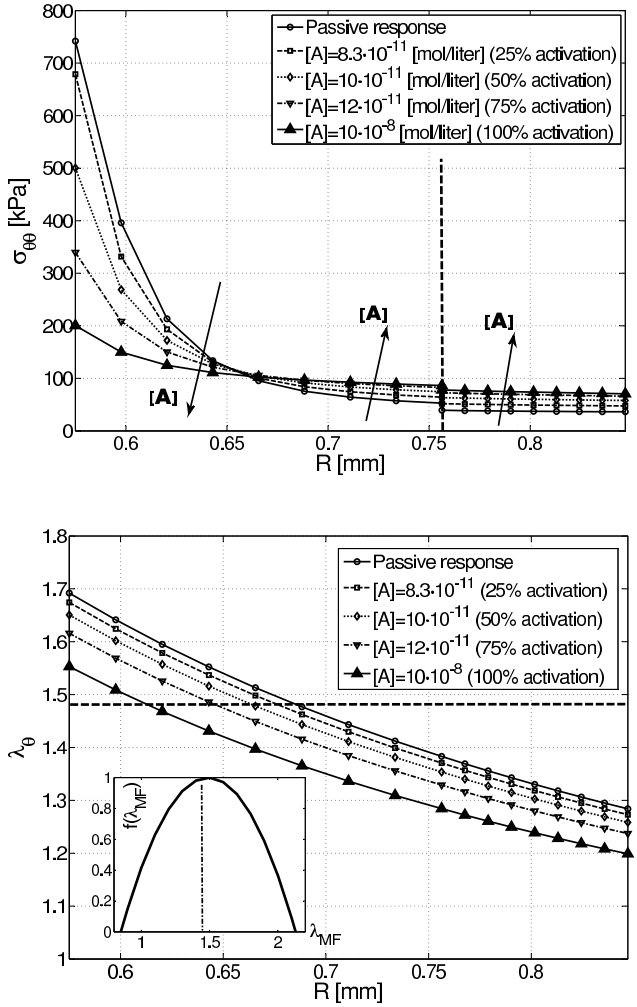

Fig. 18. Top: Circumferential Cauchy stress distribution across artery wall for different SMCs activation levels and $\beta_{MF} = 0^0, P = 100\ mmHg$. Bottom: Stretch ratio across the artery wall at $X = 5$ for different SMC activation levels, with tension-stretch relationship presented in the inner caption.

dia and across the adventitia. The contraction is inhomogeneous across the artery thickness due to the circumferential stretch ratios (in the SMC direction). In Figure 18-Bottom at $R = 0.63 - 0.67$ mm a transition for all activation levels occurs, so that the circumferential stretch ratio which is initially greater then λ_m decreases bellow λ_m. Since at the boundary of the inner media $\lambda_\theta > \lambda_m$, then as the stretch ratio decreases across the artery wall the effect of SMC contraction increases. Once a point is reached in the artery wall were $\lambda_\theta = \lambda_m$ any further decrease in λ_θ results in a decrease in the effect of SMC contraction. In Figure 19 the Cauchy stresses across the artery thickness for $\beta_{MF} = 0^0$ and $A = 10 \times 10^{-11}[mol/liter]$ for different pressures are shown. Figure 19 demonstrates that even under a constant activation level the SMC contraction is inhomogeneous across the artery thickness as a result of the different stretch ratios induced on the SMCs.

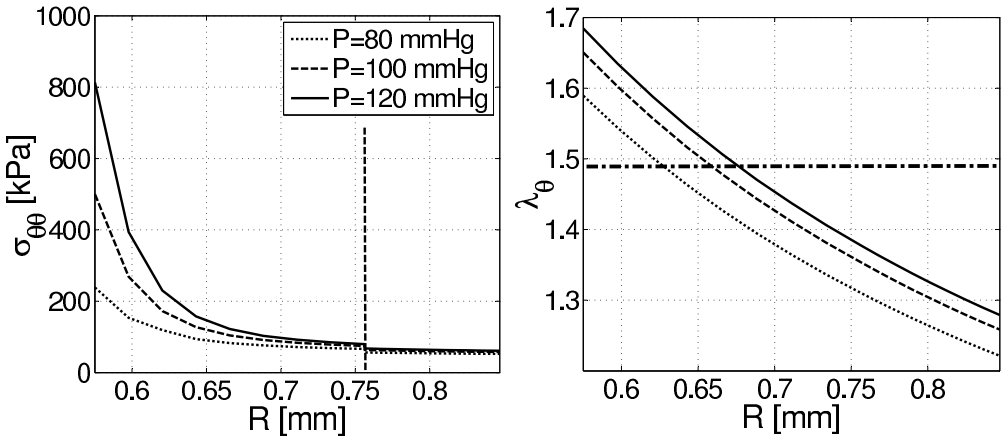

Fig. 19. Left: Circumferential Cauchy stress at $X = 5$ for different internal pressures for $\beta_{MF} = 0^0,\ [A] = 10 \times 10^{-11}[mol/liter]$, Right: Stretch ratio across the artery wall at $X = 5$ for different pressure values and $\beta_{MF} = 0^0,\ [A] = 10 \times 10^{-11}[mol/liter]$.

6 SUMMARY AND CONCLUSIONS

In [15] an anisotropic hyperelastic model, representing the passive response of the artery wall, was incorporated in the framework of the p-FEMs. Here we extended the application of p-FEMs to the passive-active response of the artery wall. A SEDF for describing the SMCs was formulated based on [7]. The ingredients required for incorporating the proposed SEDF in the finite element framework were explicitly provided. Three problems with analytical solutions used for the verification of the numerical implementation are detailed and the superiority of p-FEMs over the traditional h-FEMs for solving the coupled passive-active response was demonstrated. CPU times required to solve these nonlinear problems may be reduced by a factor of ≈ 25 and more by using the new "p-prediction" algorithm described herein.

The passive-active, tension-inflation experiments reported in [9] were used to fit both the passive and active model parameters, demonstrating that the proposed SEDF can describe the coupled passive-active response including the reduction in stress levels observed following stretches over λ_m. However, at low pressure levels (which are not physiological) our SEDF is not capable of well representing the mechanical response documented in [9]. Investigation of the active response for an artery-like structure was presented with the effect of activation level on the stresses

and deformations.

Proper description of the mechanical response of the artery wall in-vivo requires the incorporation of SMCs contribution, because experimental observations demonstrate that their activation is notable [13]. Our proposed active SEDF, although phenomenological, incorporates the distinct features of SMCs contraction as observed in experiments (tension-dose and tension-stretch relationships), and requires five material parameters $\lambda_0, \lambda_m, EC_{50}, S_{max}, m$ and one microstructural parameter β_{MF}. The active response reduces significantly the circumferential stress distribution across the artery thickness and along the artery length. The reduction in circumferential stress value is not surprising and has been reported in [7] and [10] (in both cases the tissue was assumed to be incompressible). Furthermore we observed that for high activation levels the stress gradients across the artery thickness may increase compared to moderate activation levels due to reduction of active stress generation at high stretches. On a side note, when $\beta_{MF} > 0^0$ for a constant stimulation level (not reported in this manuscript) the contraction forces which limit arterial inflation are reduced, enabling a greater arterial deformation which increases active stress generation as there is a "climb" along the tension-stretch curve provided that $\lambda_\theta < \lambda_m$. This results in an increase in both axial and circumferential stress values for increasing values of β_{MF}.

Past studies [24,25] also suggested that the stress level may drive growth and remodeling of the tissue to maintain homeostatic baseline stress values. Since we noticed that SMCs contraction largely affects the stresses, these may have a large effect on growth and remodeling. This aspect will be investigated in a future study.

With respect to the tension-stretch curve it has been shown in several studies that the value of λ_m differs greatly when different species are analyzed. In our studies based on [9] a value of $\lambda_m = 1.49$ was determined for the carotid artery of the New Zealand rabbit, whereas in [13] $\lambda_m = 1.25$ is reported for the swine carotid artery and in [8] $\lambda_m = 1.7$ and $\lambda_m = 1.62$ are reported for the human carotid artery. Some studies refer to the stress generated at the mid point of the tension-dose curve as the basal tone value as reported in [7] and more recently in [8] but since the coupling between the active and passive states is mainly dependent on the tension-stretch relation, it is reasonable to assume that basal tone values will differ from one specimen to another even if the tension-dose relation is similar.

In this study we chose to use a simple SEDF not incorporating the chemical kinetics as proposed in [11] and [26]. For models incorporating the chemical kinetics one has to determine seven different rate constants which adds to the model's complexity. The work in [12] which utilized an SEDF similar to the one proposed in [26] for modeling the experiments reported in [13] assumed a converged contraction process and as a result did not have to solve the rate equations. It is our opinion that the activation level can be properly incorporated via the tension-dose relationship when time independent problems are considered.

In our analysis we neglected both axial and circumferential residual stress as we did not want to complicate the two effects. We also assumed only one SMCs helix layer in our analysis whereas several layers with different pitch angles may exist in the media layer. The main ”bottle neck” in further research is the lack of experiments reported on the coupled response especially for human arteries. More experimental work is necessary for both passive and active parameter identification to pursue more elaborate simulations for investigation of in-vivo artery response.

One of the limitations of our study is the use of non-systematic method for the determination of the material properties. Optimization algorithms as the ones suggested by Hartmann [27] and Hollander et al. [6] will be implemented for a systematic optimization of the material parameters.

We may conclude that the SMCs-effect greatly influences the state of stress and deformation in artery walls and that p-FEMs may be utilized to investigate their passive-active response, resulting in fast and accurate results. Future work is aimed at further validating of the proposed active SEDF by experimental observation. The possibility of introducing varying active response levels for each layer based on the average volume fraction of the SMC constituents in the media and adventitia, will also be investigated. Finally, the role the active stress field plays in the pathology of vascular disease such as arteriosclerosis or the development of aneurisms may only be addressed once a validated model for the coupled mechanical response in a healthy artery will be provided.

Acknowledgements

The authors gratefully acknowledge the anonymous referees for their valuable and constructive comments, leading to improvements in the presentation and context.

References

[1] P. Chamiot-Clerc, X. Copie, J.F. Renaud, M. Safer, and X. Girerd. Comparative reactivity amd mechanical properties of human isolated internal mammary and radial arteries. *Cardiovascular Resrearch*, 37:811–819, 1998.

[2] Y.C. Fung, K. Fronek, and P. Patitucci. Pseudoelasticity of arteries and the choice of its mathematical expression. *American Journal of Physiology*, 237(5):H620–H631, 1979.

[3] A. Delfino, N. Stergiopulos, J. E. Moore, and J. J. Meister. Residual strain effects on the stress field in a thick wall finite element model of the human carotid bifurcation. *Jour. Biomech.*, 30(8):777–786, 1997.

[4] M.A Zulliger, P. Fridez, K. Hayashi, and N. Stergiopulos. A strain energy function for arteries accounting for wall composition and structure. *Jour. Biomech.*, 37(7):989–1000, 2004.

[5] G.A. Holzapfel, T.C. Gasser, and R.W. Ogden. A new constitutive framework for arterial wall mechanics and a comparative study of material models. *Jour. Elasticity*, 61:1–48, 2000.

[6] Y. Hollander, D. Durban, X. Lu, GS. Kassab, and Y. Lanir. Constitutive modeling of coronary arterial media - comparison of three model classes. *Jour. Biomech. Eng.*, 133:1–12, 2011. Article number: 061008.

[7] A. Rachev and K. Hayashi. Theoretical study of the effects of vascular smooth muscle contraction on strain and stress distributions in arteries. *Annals of Biomedical Engineering*, 27(4):459–468, 1999.

[8] I. Masson, P. Boutouyrie, S. Laurent, J.D. Humphery, and Z. Mustapha. Characterization of arterial wall mechanical behavior and stresses from human clinical data. *Jour. Biomech.*, 41:2618–2627, 2008.

[9] H.P. Wagner and J.D. Humphrey. Differential passive and active biaxial mechanical behavior of muscular and elastic arteries: Basilar versus common carotid. *Jour. Biomech. Eng.*, 133, 2011. Article number: 051009.

[10] M.A. Zulliger, A. Rachev, and N. Stergiopulos. A constitutive formulation of arterial mechanics including vascular smooth muscle tone. *Am J. Physiol. Heart Circ. Physiol*, 287:H1335–H1343, 2004.

[11] S.I. Murtada, M. Kroon, and G.A. Holzapfel. A calcium-driven mechanochemical model for prediction of force generation in smooth muscle. *Biomech. Model. Mechanobiology*, 9:749–762, 2010.

[12] A. Schmitz and M. Böl. On a phenomecnological model for active smooth muscle contration. *Jour. Biomech.*, 44:2090–2095, 2011.

[13] J.T. Herlihy and R.A. Murphy. Length-tension relationship of smooth-muscle of hog-carotid artery. *Circ. Research*, 33:275–283, 1973.

[14] S.L.M. Dahl, M.E. Vaughn, and L.E. Niklason. An ultrastructural analysis of collagen in tissue engineered arteries. *Annals Biomed. Eng.*, 35:1749–1755, 2007.

[15] Z. Yosibash and E. Priel. p-FEMs for hyperelastic anisotropic nearly incompressible materials under finite deformations with applications to arteries simulation. *Int. Jour. Numer. Meth. Engrg.*, 88:1152–1174, 2011.

[16] A. Düster, S. Hartmann, and E. Rank. p-FEM applied to finite isotropic hyperelastic bodies. *Computer Meth. Appl. Mech. Engrg.*, 192:5147–5166, 2003.

[17] Z. Yosibash, S. Hartmann, U. Heisserer, A. Duester, E. Rank, and M. Szanto. Axisymmetric pressure boundary loading for finite deformation analysis using p-FEM. *Computer Meth. Appl. Mech. Engrg.*, 196:1261 1277, 2007.

[18] U. Heisserer, S. Hartmann, A. Düster, and Z. Yosibash. On volumetric locking-free behavior of p-version finite elements under finite deformations. *Communications Numer. Meth. Engrg.*, 24(11):1019–1032, 2008.

[19] G.A. Holzapfel and R.W. Ogden. Constitutive modelling of arteries. *Proc. R. Soc. A*, 466:15511597, 2010.

[20] G.A. Holzapfel. *Nonlinear solid mechanics. A continuum approach for engineering*. John Wiley and Sons,Ltd, England, 2000.

[21] T.C. Gasser, C.A.J. Schulz-Bauer, and G.A. Holzapfel. A three dimensional finite element model for arterial clamping. *Jour. Biomech. Eng.*, 124:355–363, 2002.

[22] B. A. Szabó and I. Babuška. *Finite Element Analysis*. John Wiley & Sons, New York, 1991.

[23] C.J. Chuong and Y.C Fung. Compressibility and constitutive equation of arterial wall in radial compression experiments. *Jour. Biomech.*, 17(1):35–40, 1984.

[24] S.Q. Liu and Y.C. Fung. Indicial functions of arterial remodeling in response to locally altered blood pressure. *Heart Circ. Physiology*, 270(4):H1323–H1333, 1996.

[25] A. Rachev. Theroetical study of the effect of stress-dependent remodeling on arterial geometry under hypertensive conditions. *Jour. Biomech.*, 30(8):819–827, 1997.

[26] S.I. Murtada, M. Kroon, and G.A. Holzapfel. Modeling the dispersion effect of contractile fibers in smooth muscles. *Jour. Mech. Phys. Solids*, 58:2065–2082, 2010.

[27] S. Hartmann. Parameter estimation of hyperelasticity relations of generalized polynomial-type with constraint conditions. *Int. Jour. Solids and Structures*, 38(44–45):7999–8018, 2001.

[28] Karlsson Hibbitt and Sorensen Inc. *ABAQUS manual version 6.82EF*. 2009.

A The active SEDF assuming incompressibility

In this section we wish to demonstrate that the active SEDF provides the active Cauchy stress term given in [7] for a general incompressible deformation of the

tissue. Consider the following incompressible Cartesian deformation of the tissue embedding the SM fiber:

$$\boldsymbol{F} = \begin{bmatrix} \lambda^{-\frac{1}{2}} & 0 & 0 \\ 0 & \lambda & 0 \\ 0 & 0 & \lambda^{-\frac{1}{2}} \end{bmatrix} \Rightarrow \boldsymbol{C} = \begin{bmatrix} \lambda^{-1} & 0 & 0 \\ 0 & \lambda^{2} & 0 \\ 0 & 0 & \lambda^{-1} \end{bmatrix} \quad , \quad J(\boldsymbol{F}) = 1 \tag{A.1}$$

Where $\lambda > 1$ is the stretch of the entire tissue. The SMC are initially in the direction $\hat{\boldsymbol{M}}_{MF} = [0, \cos\beta_{MF}, \sin\beta_{MF}]$ which is not in direction of stretch. The structure tensor is:

$$\hat{\boldsymbol{M}}_{MF} \otimes \hat{\boldsymbol{M}}_{MF} = \begin{bmatrix} 0 & 0 & 0 \\ 0 & \cos^2\beta_{MF} & \cos\beta_{MF}\sin\beta_{MF} \\ 0 & \cos\beta_{MF}\sin\beta_{MF} & \sin^2\beta_{MF} \end{bmatrix} \tag{A.2}$$

Using (12) the stretch in the SMC direction is: $\lambda_f^2 = \mathrm{IV}_{\boldsymbol{C}}^{MF} = \hat{\boldsymbol{M}}_{MF}(\boldsymbol{C}\cdot\hat{\boldsymbol{M}}_{MF}) = \lambda^2\cos^2\beta_{MF} + \lambda^{-1}\sin^2\beta_{MF}$. The Cauchy stress tensor $\boldsymbol{\sigma}_{active}$ can be obtained by pushing forward $\boldsymbol{S}_{active}$ in equation (17).

$$\begin{aligned} \boldsymbol{\sigma} &= \frac{1}{J}\boldsymbol{F}\boldsymbol{S}\boldsymbol{F}^T \\ &= \begin{bmatrix} \lambda^{-\frac{1}{2}} & 0 & 0 \\ 0 & \lambda & 0 \\ 0 & 0 & \lambda^{-\frac{1}{2}} \end{bmatrix} \begin{bmatrix} 0 & 0 & 0 \\ 0 & \lambda & 0 \\ 0 & 0 & \lambda^{-\frac{1}{2}} \end{bmatrix} \cdot S^* \\ &= \begin{bmatrix} 0 & 0 & 0 \\ 0 & \lambda^2\cos^2\beta_{MF} & \lambda^{\frac{1}{2}}\cos\beta_{MF}\sin\beta_{MF} \\ 0 & \lambda^{\frac{1}{2}}\cos\beta_{MF}\sin\beta_{MF} & \lambda^2\sin^2\beta_{MF} \end{bmatrix} \cdot S^* \end{aligned} \tag{A.3}$$

With $S^* = S([A])f(\mathrm{IV}_{\boldsymbol{C}}^{MF})\left(\mathrm{IV}_{\boldsymbol{C}}^{MF}\right)^{-\frac{1}{2}}$.
The unit vector in the SMC direction after the deformation is:

$$\hat{\boldsymbol{m}}_{MF} = \frac{\boldsymbol{m}_{MF}}{|\boldsymbol{m}_{MF}|} = \frac{\boldsymbol{F}\hat{\boldsymbol{M}}_{MF}}{\sqrt{\boldsymbol{F}\hat{\boldsymbol{M}}_{MF}\cdot\boldsymbol{F}\hat{\boldsymbol{M}}_{MF}}} = \begin{bmatrix} 0 \\ \lambda\cos\beta_{MF} \\ \lambda^{-\frac{1}{2}}\sin\beta_{MF} \end{bmatrix} \cdot \frac{1}{\sqrt{\mathrm{IV}_{\boldsymbol{C}}}} \tag{A.4}$$

Thus the component of the Cauchy stress in the SMC direction is:

$$\sigma_{MF} = (\boldsymbol{\sigma} \cdot \hat{\boldsymbol{m}}_{MF}) \cdot \hat{\boldsymbol{m}}_{MF} = S^{*} \mathrm{IV}_{\boldsymbol{C}}^{MF} = S([A]) f(\mathrm{IV}_{\boldsymbol{C}}^{MF}) \sqrt{\mathrm{IV}_{\boldsymbol{C}}} = S([A]) f(\lambda_f) \lambda_f \tag{A.5}$$

This is in accordance with the expression for the Cauchy stress provided in [7] for a stretch in the SMC direction.

B Derivation of the body force term for problem C

The equilibrium equations in Cartesian coordinates are:

$$\frac{\partial \sigma_{ij}}{\partial x_i} = f_j \rightarrow \frac{\partial \sigma_{ij}}{\partial X_k} \frac{\partial X_k}{\partial x_i} = f_j \rightarrow \frac{\partial \sigma_{ij}}{\partial X_k} F_{ki}^{-1} = f_j \tag{B.1}$$

The Cauchy stress tensor is computed by $\boldsymbol{\sigma} = \frac{1}{J} \boldsymbol{F} \boldsymbol{S} \boldsymbol{F}^T = \frac{2}{J} \boldsymbol{F} \frac{\partial \Psi}{\partial \boldsymbol{C}} \boldsymbol{F}^T$. With the deformation gradient $\boldsymbol{F}$ and left Cauchy-Green deformation tensor $\boldsymbol{C}$ for problem C given as:

$$\boldsymbol{F} = \begin{bmatrix} 1 & 0 & 0 \\ 0 & 1 & 0 \\ 0 & 0 & Z^{\frac{1}{2}} \end{bmatrix} \Rightarrow \boldsymbol{C} = \begin{bmatrix} 1 & 0 & 0 \\ 0 & 1 & 0 \\ 0 & 0 & Z \end{bmatrix} \Rightarrow \boldsymbol{C}^{-1} = \begin{bmatrix} 1 & 0 & 0 \\ 0 & 1 & 0 \\ 0 & 0 & Z^{-1} \end{bmatrix} \quad , \quad J = \det \boldsymbol{F} = Z^{\frac{1}{2}} \tag{B.2}$$

Using equations (4)(6)(15) one can obtain an expression for $\boldsymbol{S}$ in the form:

$$\begin{aligned} \boldsymbol{S} = {} & Z^{-\frac{1}{3}} c_1 \left(-\frac{2}{3} \boldsymbol{C}^{-1} (2 + Z) + 2\boldsymbol{I} \right) + \frac{2}{D_1} \boldsymbol{C}^{-1} \left(Z - Z^{-\frac{1}{2}} \right) \\ & + S([A]) \left(\mathrm{IV}_{\boldsymbol{C}}^{MF} \right)^{-\frac{1}{2}} \left(1 - \left(\frac{\lambda_m - \sqrt{\mathrm{IV}_{\boldsymbol{C}}^{MF}}}{\lambda_m - \lambda_0} \right)^2 \right) \left[\hat{\boldsymbol{M}}_{MF} \otimes \hat{\boldsymbol{M}}_{MF} \right] \end{aligned} \tag{B.3}$$

With $\hat{\boldsymbol{M}}_{MF} = [0, 0, 1]$ and $\mathrm{IV}_{\boldsymbol{C}}^{MF} = \left[\hat{\boldsymbol{M}}_{MF} \otimes \hat{\boldsymbol{M}}_{MF} \right] : \boldsymbol{C} = Z$. The Cauchy stress takes the form:

$$\begin{aligned} \boldsymbol{\sigma} = {} & Z^{\frac{1}{6}} c_1 \left(-\frac{2}{3} \boldsymbol{C}^{-1} (2 + Z) + 2\boldsymbol{I} \right) + \frac{2}{D_1} \boldsymbol{C}^{-1} \left(Z^{\frac{3}{2}} - 1 \right) \\ & + S([A]) \left(1 - \left(\frac{\lambda_m - \sqrt{Z}}{\lambda_m - \lambda_0} \right)^2 \right) \left[\hat{\boldsymbol{M}}_{MF} \otimes \hat{\boldsymbol{M}}_{MF} \right] \end{aligned} \tag{B.4}$$

Using (B.1) and (B.4) the body force component required to maintain equilibrium can be computed.

$$
\begin{aligned}
f_x &= -\left(\frac{\partial \sigma_{xx}}{\partial x} + \frac{\partial \sigma_{yx}}{\partial y} + \frac{\partial \sigma_{zx}}{\partial z}\right) = 0 \\
f_y &= -\left(\frac{\partial \sigma_{xy}}{\partial x} + \frac{\partial \sigma_{yy}}{\partial y} + \frac{\partial \sigma_{zy}}{\partial z}\right) = 0 \\
f_z &= -\left(\frac{\partial \sigma_{xz}}{\partial x} + \frac{\partial \sigma_{yz}}{\partial y} + \frac{\partial \sigma_{zz}}{\partial z}\right) = -\frac{\partial \sigma_{zz}}{\partial z} = -\frac{\partial \sigma_{zz}}{\partial Z}\frac{\partial Z}{\partial z} = \\
&\quad -\frac{4c_1}{18}Z^{-\frac{4}{3}} - \frac{20c_1}{18}Z^{-\frac{7}{3}} - \frac{1}{D_1 Z} - S([A])\left(\frac{\lambda_m - \sqrt{Z}}{\lambda_m - \lambda_0}\right)Z^{-1}
\end{aligned}
\tag{B.5}
$$

C Comparison of our code to Abaqus using h-extension

Here we wish to compare between the performance of our code and the commercial code Abaqus [28] when h-extension is used. To that end we use problem C given in Table 1 but with no SMC contribution (not available in Abaqus) similar to the problem presented in [15]. In Abaqus an automatic load stepping was used resulting in 17 load increments with an average of 3 equilibrium iterations per a step. In our code we used 20 equal load steps resulting in an average of three equilibrium iterations per step. In Figure C.1 the relative error in u_Z and σ_{ZZ} extracted at point $X = 2, Y = 2, Z = 2$ is compared as a function of CPU using both our code and Abaqus. It can be seen that both our code and Abaqus cannot converge to the exact solution when only $p = 1$ is utilized for the h-extension used (8 to 1000 elements). When stresses are considered both codes reached a minimum relative error of $\sim 3.5\%$. In terms of CPU times Abaqus requires shorter CPU times up to a factor of ≈ 2.5 for the h-extension considered. This can be attributed in part to the automatic load stepping algorithm implemented in Abaqus and not yet implemented in our code. It should be noted however that when p-extension is considered for the same problem and p-FEM is compared to h-FEM our code out performs Abaqus as demonstrated in [15].

D Simulation of uniaxial extension experiments

In this section we wish to demonstrate that our proposed SEDF can model the reduction in active force generation observed in uniaxial-extension experiments reported in [13]. Finite element models simulating the uniaxial stretch-tension experiments were generated. The boundary conditions and mesh used for computation are shown in Figure D.1.

Remark 4 *It is reported in [13] that examination of the tissue showed that the SMCs are arranged in a helix like structure with a pitch of angle $\theta = 4.5^0$ with*

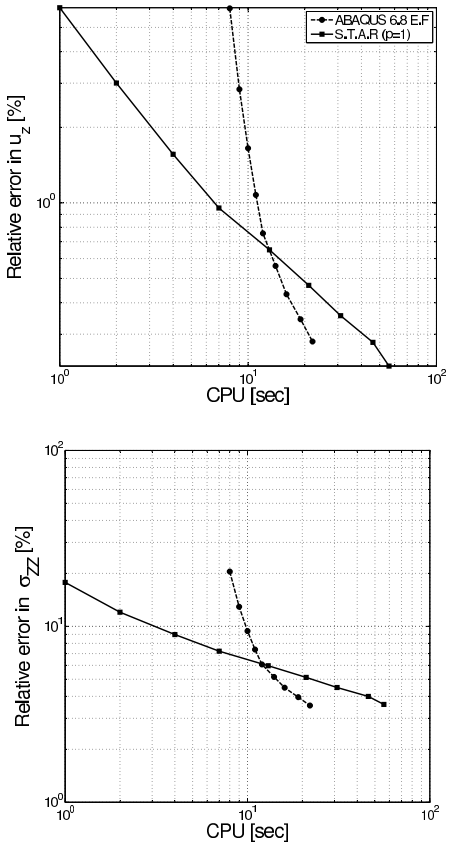

Fig. C.1. Relative error in displacement and stress using our code and Abaqus 6.8 E.F.

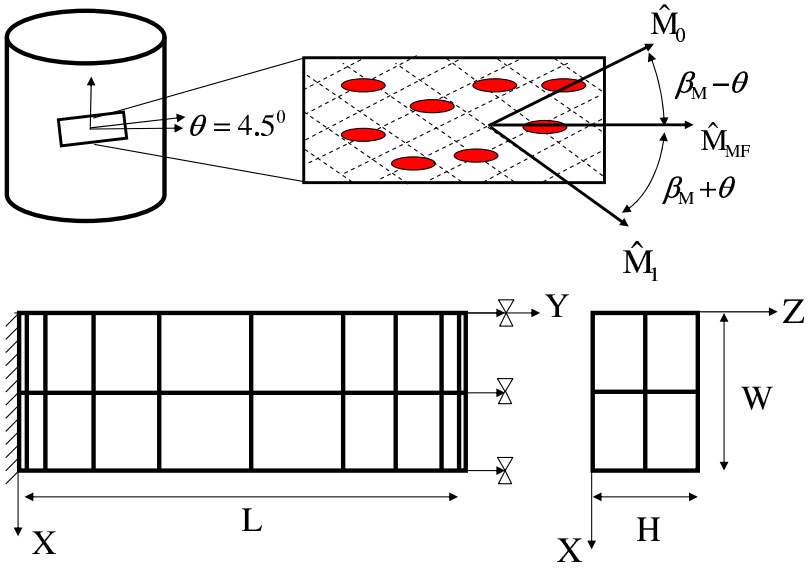

Fig. D.1. Boundary conditions and mesh for the uniaxial tension of an arterial strip.

respect to the circumferential direction. The specimens were cut so as to have the SMCs aligned with the extension direction and therefore in our FE model the col-

lagen fibers families are not symmetric with respect to the stretch direction as depicted in Figure D.1.

All analyses for the fitting process were conducted using $p = 4$ following convergence tests for which $|||e(\mathcal{U})|| < 0.1\%$. Displacement boundary conditions were specified at one end of the strip while the other end was clamped and a constant value $[A] = 0.005\ [mol/liter]$ was applied as reported in [13]. The fitted material parameters and stress-stretch response for both passive and active states are given in Table D.1 and Figure D.2 respectively. As evident from Figure D.2 the proposed active SEDF is capable of predicting the softening branch of the active curve following $\lambda > \lambda_m$.

Table D.1
Material parameters fitted to a slightly compressible passive-active SEDF.

c_1 $[MPa]$	D_1 $[MPa^{-1}]$	k_1 $[MPa]$	k_2	β_M $[^0]$	λ_0	λ_1	λ_m	m	EC_{50} $[mol/liter]$	S_{max} $[kPa]$
0.007	2	0.025	4.3	± 35	0.4	2.1	1.25	1	0.00075	222

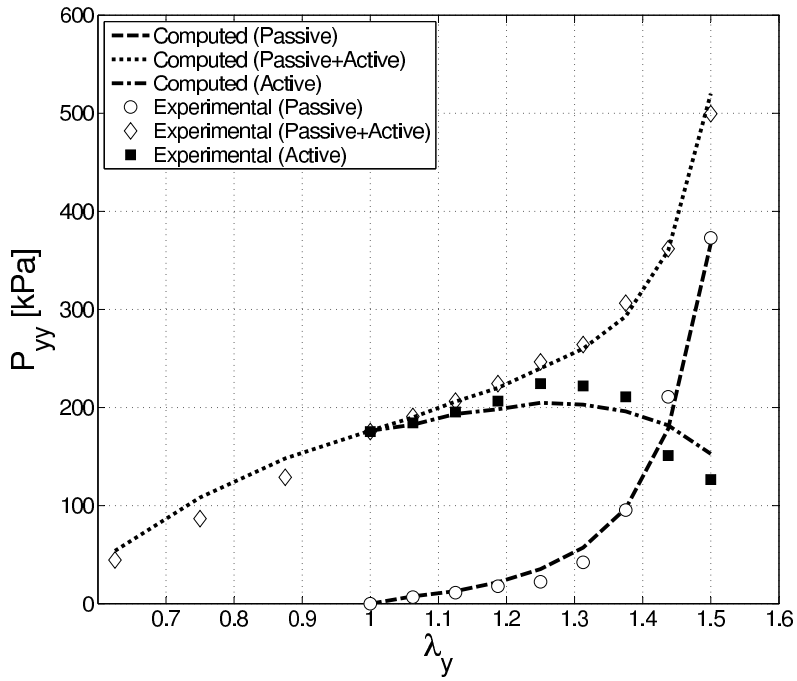

Fig. D.2. Stress-stretch relationship for a swine carotid media strip - Model and experiments from [13] for pure passive and coupled passive-active state, $[A] = 0.005\ [mol/liter]$.